Microstructural Defects in Antimony Selenide Solar Cells

RHYS EDWARD WILLIAMS

Microstructural Defects in Antimony Selenide Solar Cells

Rhys E. Williams

Submitted for the degree of Master of Science by Research

2019

Abstract

Antimony selenide (Sb_2Se_3) is an emerging photovoltaic material that has attracted attention not only because of its low-toxicity, earth abundant composition, but also because of its unusual one-dimensional nano-ribbon crystal structure, which has the potential to eliminate recombination losses at grain boundaries.

In this project, electron microscopy analysis was carried out on three devices grown by thermal evaporation (TE) and close space sublimation (CSS) on CdS and TiO_2 emitter layers, as well as a seed layer grown by CSS on TiO_2, in order to better understand differences in performance between the three devices.

Scanning electron microscopy and scanning transmission electron microscopy cross-sectional images of the devices showed that the device grown by CSS on CdS had voids around 300 nm thick across almost the entire width of the CdS-Sb_2Se_3 interface. Energy dispersive X-ray spectroscopy showed that this was likely due to Kirkendall voiding, caused by the diffusion of Se and Sb into the CdS layer. This diffusion also led to Se being substituted for S to form a Cd(S,Se) layer, which reduced external quantum efficiency, and may also form a charge transport barrier at the heterojunction. These effects would account for the low ($\approx 1\%$) efficiency of this device.

Analysis of electron diffraction patterns and high resolution electron micrographs allowed the orientation of the Sb_2Se_3 nano-ribbons relative to the film thickness direction to be measured for individual grains. For all devices the mean orientations were within one standard deviation of each other, at around 30-50°. This is consistent with X-ray diffraction patterns reported in the literature. For the device grown on TiO_2 by CSS, a correlation was found between grain size and orientation: the largest grains had ribbons more normal to the substrate. This may be due to the influence of the seed layer, and may in part account for this sample having the highest efficiency ($\approx 6\%$).

Microstructural Defects in Antimony Selenide Solar Cells

Rhys Edward Williams

A Thesis presented for the degree of

Master of Science by Research

Contents

List of Figures

List of Tables

List of Abbreviations

CIGS Copper Indium Gallium Diselenide. 22, 23

CSS Close-Space Sublimation. 1, 13, 24, 26, 27, 28, 29, 44, 45, 55, 61, 64, 72, 74, 75, 76, 77

EDX Energy Dispersive X-ray spectroscopy. 27, 29, 43, 48, 55, 58, 59, 60, 63, 64, 65, 67, 68, 70, 71, 77

EQE External Quantum Efficiency. 13, 71, 72

FEG Field Emission Gun. 31, 36, 46

FIB Focused Ion Beam. 35, 36, 37, 56, 61, 64, 68, 70

FIB SEM Focused Ion Beam Scanning Electron Microscope. 27, 35, 36, 37, 46

FTO Fluorine Doped Tin Oxide. 44, 47, 55, 58, 61, 64, 65, 68, 71

HAADF High Angle Annular Dark Field. 42, 43, 77

HREM High Resolution Electron Microscopy. 27, 29, 41, 51, 52, 57, 58, 62, 64, 75, 77

HTL Hole Transport Layer. 24

LMIS Liquid Metal Ion Source. 36

RTE Rapid Thermal Evaporation. 24, 26, 27

SEM Scanning Electron Microscopy. 31, 32, 33, 35, 36, 37, 38, 39, 42, 43, 46, 55, 56, 61, 64, 65, 68

SIMS Secondary Ion Mass Spectrometry. 29

SLME Spectroscopic Limited Maximum Efficiency. 21, 24

Declaration

The work in this thesis is based on research carried out in the Department of Physics, Durham University, United Kingdom. No part of this thesis has been submitted elsewhere for any other degree or qualification and it is all my own work unless referenced or stated to the contrary in the text with the exceptions listed below.

Device growth, measurement of performance parameters, and EQE and XRD analysis of the CdS - CSS Sb_2Se_3 device was carried out by Laurie Phillips, University of Liverpool.

Device growth, measurement of performance parameters, and EQE and XRD analysis of the CdS - TE Sb_2Se_3 device was carried out by Peter Yates, University of Liverpool.

Device growth, measurement of performance parameters, and EQE and XRD analysis of the TiO_2 - CSS Sb_2Se_3 device and seed layer was carried out by Oliver Hutter, University of Liverpool.

Acknowledgements

Thanks are first due to my supervisor, Dr. Budhika Mendis, for all of his patience and support.

I should also thank Dr. Jon Major for being informative and helpful on the subject of antimony selenide solar cells. Thanks also to Laurie Phillips, Peter Yates and Oliver Hutter for growing these devices and providing me with whatever data I asked them for.

Chapter 1

Introduction

Climate change necessitates the development of renewable energy sources. As shown in Figure 1.1 the planet is currently on course for at least 1° C, possibly as much as 4° C of warming by the end of the century. This is expected to have significant negative effects, and is widely accepted to be caused by human activity releasing greenhouse gases into the atmosphere, most notably the emission of CO_2 by the burning of fossil fuels [1]. Figure 1.2 shows greenhouse gas emissions in the EU for the year 2014 broken down by sector. Presently, around 29% of CO_2 emissions in the EU are from energy generation, and demand for electricity will only increase as it is increasingly used to power vehicles and heat homes [2].

This makes the development of renewable energy critical to avoiding large-scale climate change. The large amount of sunlight falling on the earth makes solar one of the most attractive renewable energy options: the quantity of solar power reaching the surface of the planet far exceeds global energy demand (6500 TW compared to 12.5 TW) [3, 4]. Accordingly, over the past 20 years photovoltaic peak power capacity has increased massively from negligible levels to near 100 GW per year [5].

1.1 Theory of Solar Cells

1.1.1 pn Junctions

Most solar cells are based upon a pn junction, illustrated in Figure 1.3 [6], where the p-type material is the absorber layer and the n-type material is known as the emitter layer. In a p-type semiconductor holes are the majority charge carriers, and an n-type material has electrons as the majority charge carriers. At the metallurgical junction between these two
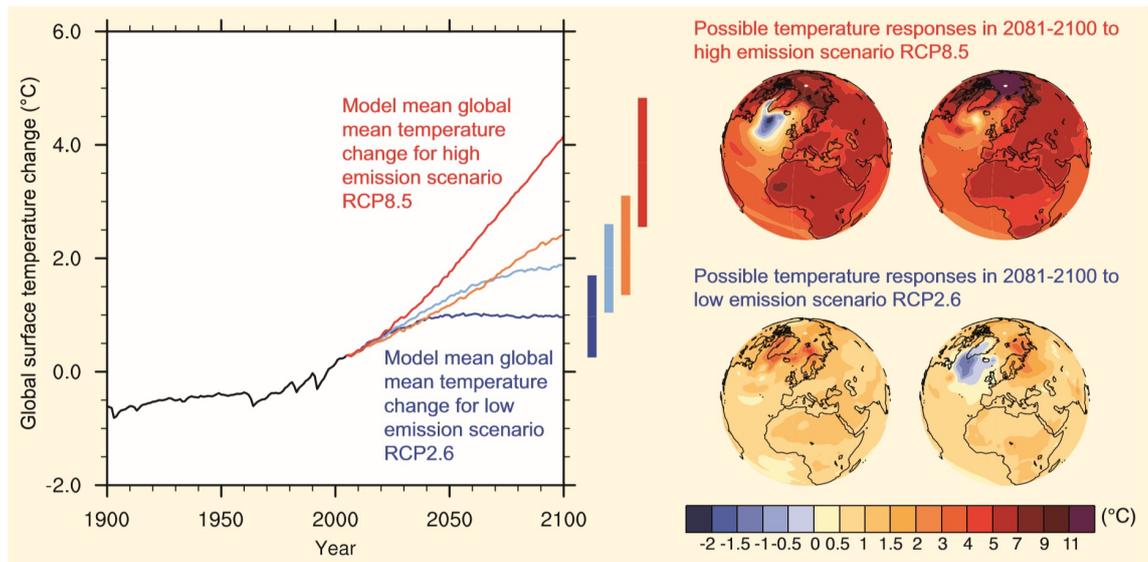
Figure 1.1: Global mean temperature change predictions for the year 2100, according to four emissions scenarios defined by the IPCC. The coloured bars indicate the uncertainty for each scenario [1].
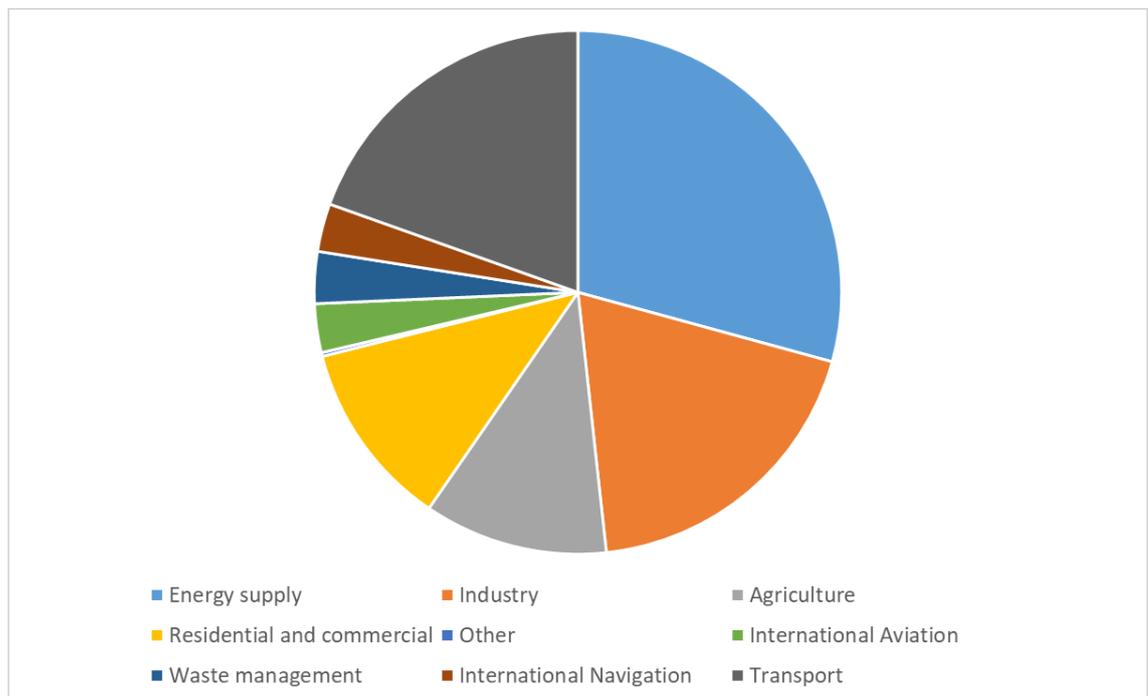
Figure 1.2: Greenhouse gas emissions across the EU for the year 2014, broken down by sector [2].
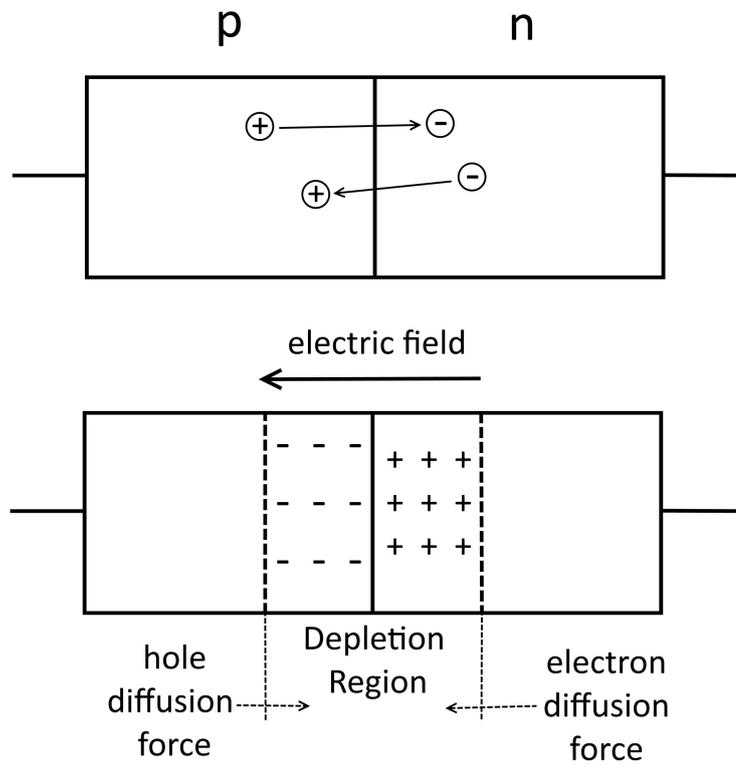
Figure 1.3: Diagram showing the formation of the space charge region about a pn junction.
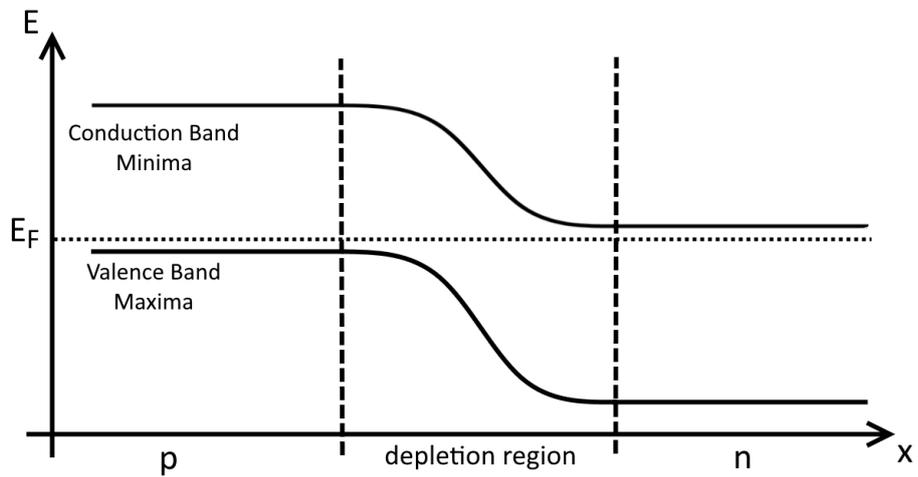
Figure 1.4: Energy band diagram showing variation in valence band maxima and conduction band minima across a pn junction.

types of material, free electrons will flow from the n-type to p-type material and recombine with the majority carrier holes there, and free holes will flow the other way to recombine with the electrons in the n-type material. The recombination of these free charge carriers leaves a net positively charged region in the n-type material, and a negatively charged region in the p-type material which are essentially depleted of free charge carriers. Together these are known as the depletion region or space charge region.

When the junction reaches equilibrium, the potential difference between the positively and negatively charged regions induces an electric field which drives a current that cancels out the current arising from the diffusion of charge carriers across the junction [7]. The Fermi levels of the two materials will then be equal, which causes the conduction and valence band edges to bend in order to compensate for the difference in work function between the two sides of the junction (Figure 1.4 [6]. This is the basis of the charge separation mechanism necessary for the function of photovoltaic devices [8].

1.1.2 Generation

The primary generation process in photovoltaic materials is photogeneration- the generation of mobile charge carriers by the absorption of light in the semiconductor. Consider a direct bandgap semiconductor, having bandgap E_g. A photon having energy $h\nu < E_g$ will pass through the material without being absorbed, having insufficient energy to promote an electron from the valence to the conduction band. In contrast, in an ideal situation, a photon having energy $h\nu > E_g$ will be absorbed, giving up its energy to promote an electron into the conduction band, and generating an electron-hole pair. This electron will then relax to the bottom of the conduction band, giving up surplus energy as thermal energy [8]. As E_g decreases, the total number of photons absorbed will increase; however increasing amounts of energy will be lost thermally. It follows that there is an optimum bandgap corresponding to a maximum theoretical efficiency for a solar cell based on a single pn junction. This is known as the Shockley-Queisser limit, and corresponds to a solar conversion efficiency of 44% at 1.1 eV for a 6000 K black-body [9], or 33.7% at a bandgap of 1.34 eV for the AM 1.5 solar spectrum [10], but varies with temperature and atmospheric conditions [11, 12].
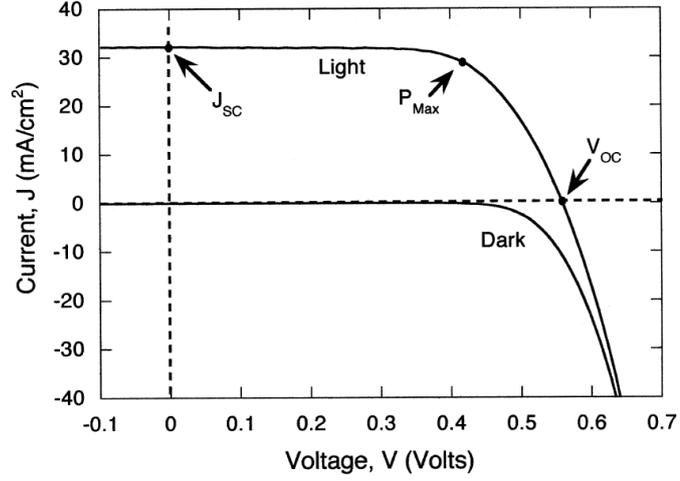
Figure 1.5: Typical $J - V$ curves for a solar cell operating in the dark and under illumination. On the illumintation curve V_{OC}, J_{SC} and the maximum power point P_{Max} are shown [13].

1.1.3 Charge Separation and Device Parameters

The electric field at the pn junction drives photogenerated electrons and holes to opposite terminals of the cell, creating a potential difference between them. The open circuit voltage, V_{OC}, is the value of this potential difference when the cell is under infinite load resistance (i.e. not connected to a circuit). The short circuit current density, J_{SC}, is the current that will flow when the cell is under zero load resistance (i.e. the two terminals connected together) per unit area illuminated [6,8,13]. These parameters are shown on a typical $J - V$ curve for a solar cell in Figure 1.5. J_{SC} is given by,

$$J_{SC} = q \int b_s(E) QE(E) dE \tag{1.1.1}$$

where q is the charge of an electron, b_s the incident spectral photon flux density (defined as the number of photons having energy in the range E to $E + dE$ which are incident on the cell per unit area per unit time), and QE is the quantum efficiency (defined as the probability that an incident photon of energy E will cause an electron to move through the circuit) [6,13].

The total cell current density $J(V)$ for a given voltage V is approximated by the sum of J_{SC} and the dark current density, J_{dark}. The form of $J(V)$ and J_{dark} are shown in Figure 1.5. The dark current is the current generated by the voltage between the two terminals

which flows in the opposite direction to the photocurrent. J_{dark} is given by [6, 13],

$$J_{dark}(V) = J_o(e^{qV/k_B T} - 1)$$

Therefore, for an ideal diode,

$$J(V) = J_{SC} - J_o(e^{qV/k_B T} - 1) \tag{1.1.2}$$

where J_o is the reverse saturation current density, k_B is the Boltzmann constant, and T is temperature [13]. The open circuit voltage is the maximum possible voltage given by the cell and occurs in the situation where J_{dark} cancels J_{SC}. Therefore, by rearranging Equation (1.1.2) an expression for V_{OC} is obtained [6, 13],

$$V_{OC} = \frac{kT}{q} \ln \left(\frac{J_{SC}}{J_o} + 1 \right) \tag{1.1.3}$$

The power density of the cell is given by $P = JV$ and would be at its maximum at $V = V_{OC}$, $J = J_{SC}$ for a device with a perfectly square $J - V$ curve. In reality, the maximum power point P_{Max}, shown in Figure 1.5, occurs at V_m and J_m. The fill factor, FF, is defined as,

$$FF = \frac{J_m V_m}{J_{SC} V_{OC}} \tag{1.1.4}$$

and is a measure of how close to square the JV curve is [6, 13]. The efficiency of the cell is then given by,

$$\eta = \frac{J_{SC} V_{OC} FF}{P_s} \tag{1.1.5}$$

where P_s is the incident light power density. J_{SC}, V_{OC}, FF, and η are the four values commonly given as measures of the performance of a cell [6, 13].

There are two parasitic resistances impacting the performance of the cell: the series resistance R_s, which arises from the resistance of the cell to current flow (e.g. cell layer and contact resistance); and the shunt resistance R_{sh}, which is the resistance of the cell to current leaking across the junction (i.e. Ohmic versus rectifying junction behaviour). With these resistances taken into account, the diode equation becomes,

$$J = J_{SC} - J_o(e^{q(V+JAR_s)/kT} - 1) - \frac{V + JAR_s}{R_{sh}} \tag{1.1.6}$$

where A is the illuminated area of the cell. It is clear from this equation that in order to optimise the performance of the cell R_{sh} must be maximised and R_s must be minimised [6, 13].

1.1.4 Limits to Efficiency

An approximate thermodynamic limit to efficiency can be obtained by treating a solar cell as a Carnot cycle acting between the sun at 5800 K and the environment at 300 K, which gives a result of 95% efficiency. In reality, the maximum thermodynamic efficiency is slightly lower at 93% due to solar radiation being an irreversible process [14].

This thermodynamic limit is much higher than the Shockley-Queisser limit given above, which is calculated using the principle of detailed balance, i.e. the rate of photon absorption by the cell must be equal to the rate of photon emission by the cell. To achieve the detailed balance limit for $h\nu > E_g$, $QE = 1$, and the only recombination process must be radiative recombination, i.e. an electron emitting a photon as it relaxes from the conduction to the valence band. The Shockley-Queisser limit is the maximum theoretical efficiency for a single junction, planar solar cell [9].

Many materials with an optimal bandgap according to the Shockley-Queisser limit have however been found to perform poorly as photovoltaic materials. The spectroscopic limited maximum efficiency (SLME) develops the idea of the Shockley-Queisser limit, but takes into account that E_g may be direct or indirect, and that the lowest direct transition may be dipole forbidden, in order to give a more accurate prediction of photovoltaic performance. Although Shockley-Quiesser assumes that all recombination is radiative, if the lowest bandgap is not direct and dipole allowed this may not be the case, and other mechanisms such as Auger recombination may dominate. SLME takes this into account by setting the fraction of radiative recombination current $f_r = e^{-\delta/kT}$, where δ is the difference between the bandgap and the lowest allowed direct transition. Additionally, while Shockly-Queisser assumes that absorption is 1 for $h\nu > E_g$, and 0 for $h\nu < E_g$, the SLMEreplaces this with a function $a = 1 - e^{2\alpha(E)L}$, where $\alpha(E)$ is the absorption coefficient, and L is the cell thickness [15].

As an example of the difference between the Shockley-Queisser limit and the SLME, AgInTe$_2$ and CuYTe$_2$ both have bandgaps close to 1.17 eV [15], corresponding to a Shockley-Queisser limit of 32.74% [10], yet have SLME values of 27.6% and 7.5%, repsectively [15]. It is possible to exceed SLME and Shockley-Queisser limits using multijunction cells,

with the limiting efficiency for a device having an infinite number of junctions being 86.8% [16].

1.2 Thin-film Solar cells

The current dominant solar cell technologies are those based on crystalline silicon, accounting for over 90% of capacity [5], and are capable of good efficiencies (27.6% for single-crystal silicon [17]). Unfortunately these devices are costly and difficult to manufacture, and because silicon is an indirect bandgap material [18] it is a relatively poor absorber of light, meaning that silicon devices need to be relatively thick in order to achieve good efficiencies.

Thin-film devices are based on materials which absorb light more strongly (often direct bandgap materials) and so can be made several times thinner, reducing weight and costs. In addition, these materials can achieve good efficiencies from polycrystalline thin-films which can be quickly and easily deposited. This is in contrast to silicon cells, which require clean-room processing of wafers cut from silicon ingots. Some thin-film materials already exceed market leader multicrystalline silicon in laboratory efficiencies [17]. The leading thin-film materials are cadmium telluride (CdTe) and copper indium gallium diselenide (CIGS).

As of 2017 CdTe was the dominant thin-film technology, having a share of the global solar market of 2.3% [5]. CdTe has a direct bandgap of 1.44 eV, which is close to the optimum value for photoconversion, and allows it to absorb almost all visible light within 1 μm [19]. The typical design is an n-CdS, p-CdTe heterojunction, with the CdS acting as a thin window layer [6, 8, 19]. Two main factors affecting the efficiency of the CdTe cell are that the CdS layer strongly absorbs green-blue light and must be made as thin as possible, and the high number of trap states and recombination centres arising due to dangling bonds at grain boundaries, leading to high recombination losses [6, 21]. In spite of this, relatively high efficiencies are still achievable, with the record laboratory device having an efficiency of 22.1% [17]. The most significant issue facing CdTe cells is concern about the high toxicity of cadmium and the hazards that this creates in manufacturing and disposing of cells [6, 8].

CIGS is a direct bandgap material, and has a very high optical absorption coefficient. By varying the ratio of indium to gallium within the material it is possible to vary the bandgap of the material between 1.04 and 1.67 eV. Because of the process by which the material is grown, this ratio is not constant throughout the thickness of the device, leading
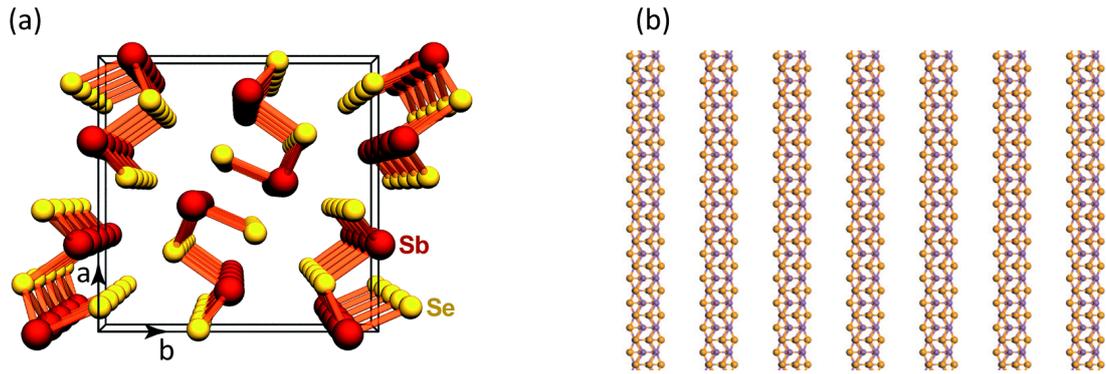
Figure 1.6: The crystal structure of antimony selenide. (a) Sb_2Se_3 unit cell, smaller yellow atoms are Se, larger red atoms are Sb. (b) Sb_2Se_3 nanoribbons, orange atoms are Sb, purple are Se [20, 27].

to bandgap grading which improves the performance of the device. High efficiency devices have an effective bandgap of 1.1 to 1.2 eV [22]. These devices consist of a p-type CIGS layer and an n-type CdS layer, often with a high resistance ZnO coating. Similar to CdTe, CIGS suffers from trap states and recombination centres arising from defects at grain boundaries [6, 23, 24]. CIGS has achieved the highest efficiency of all established thin-film technologies, with a record of 22.9% [17], and as of 2017 had a global market share of 1.9% [5]. The largest obstacle to widespread usage of CIGS for power generation is the relative scarcity of indium (comparable to silver), leading to a high materials cost [6, 8, 22].

1.2.1 Antimony Selenide (Sb_2Se_3)

Antimony Selenide (Sb_2Se_3) is a material which has attracted interest in recent years for two main reasons; the first is that, in contrast to CdTe and CIGS it is composed of low-toxicity, relatively abundant elements [25, 26]; the second is its unusual crystal strucutre, illustrated in Figure 1.6. The material is composed of 1D ribbons, oriented along the c-axis, joined by Van der Waals bonds in the a and b directions [27, 28]. The effect of this is that provided the grains are correctly oriented, the grain boundaries will lie parallel to the Van Der Waals gaps between the ribbons, thus avoiding the dangling covalent bonds which limit efficiency in other materials [21, 23, 24]. This highlights the importance of orientation control in the growth of this material; should the ribbons be poorly oriented (e.g. lying flat relative to the substrate), not only will the benign grain

boundaries be lost, but the charge carriers will have to travel across the Van der Waals gaps, increasing series resistance in the cell [27, 29].

Beyond these factors, Sb_2Se_3 has a high absorption coefficient ($> 10^{-5}$ cm^{-1}) close to the absorption onset [26, 30], and is a stable fixed phase material [31]. The material has a bandgap of around 1.1-1.2 eV [31–36], close to the ideal for a Shockley-Queisser limit of 30% [9, 37]. Experimental work has measured the indirect band gap as being 1.03 ± 0.01 eV, and the direct bandgap as being 1.17 ± 0.02 eV [31]; whilst more recent simulation work has calculated the indirect bandgap to be 1.299 eV, and the direct gap as being 1.324 eV. From these latter values the spectroscopic limited maximum efficiency (SLME) has been calculated as 28.2% for a 200 nm thick film of this material, which in spite of the indirect bandgap is superior to CdTe, having an SLME of 20.3% [38].

Antimony selenide cells have been prepared by a variety of methods and in a variety of configurations [26–28, 31, 37–41]. One of the earliest significant results was a hydrazine processed cell in superstrate configuration with a TiO_2 emitter layer, having an efficiency of 2.26% ($V_{oc} = 0.52$ V, $J_{sc} = 10.3$ mA cm^{-2}, FF = 42.3%), which was reported in 2014 [26]. The toxic nature of hydrazine, however, encouraged researchers to explore other growth techniques. Since then, many of the most significant advances in efficiency have been in cells produced via physical vapour deposition processes, such as thermal evaporation (TE) and close-space sublimation (CSS). In the same year, a cell grown using TE in superstrate configuration on CdS was reported, having an efficiency of 1.9% ($V_{oc} = 0.3$ V, $J_{sc} = 13.2$ mA cm^{-2}, FF = 48%) [39]. Since then development has been rapid. An efficiency of 6.5% ($V_{oc} = 0.427$ V, $J_{sc} = 25.5$ mA cm^{-2}, FF = 59.3%) was achieved in 2017 for a cell in superstrate configuration with a CdS emitter layer grown by rapid thermal evaporation (RTE). This cell made use of PbS colloidal quantum dots to form a hole transport layer (HTL) at the back contact, effectively giving the device a p-i-n structure [37].

This was followed in 2018 by another cell in superstrate configuration with a CdS layer, this time grown by a vapour transport deposition process. This cell achieved an efficiency of 7.6% ($V_{oc} = 0.42$ V, $J_{sc} = 29.9$ mA cm^{-2}, FF = 60.4%) [40]. The highest efficiency reported to date is 9.2% ($V_{oc} = 0.4$ V, $J_{sc} = 32.58$ mA cm^{-2}, FF = 70.3%) [41]. This device was grown by CSS and had a CdS emitter layer; however in contrast to the other devices it was grown in substrate configuration and utilised a thin layer of TiO_2 between the CdS and the Sb_2Se_3 to prevent diffusion of Sb into the emitter layer. This diffusion
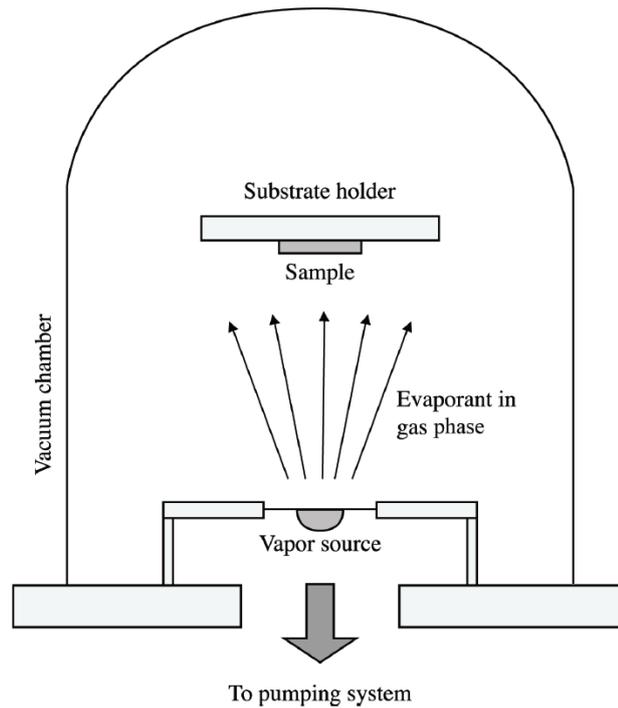
Figure 1.7: Schematic of a typical thermal evaporation setup [46].

was believed to occur due to the partial dissolution of the Sb_2Se_3 during the chemical bath deposition of the CdS layer [41]. Cells grown by CSS and RTE have also shown interdiffusion between the CdS and Sb_2Se_3 layers, which often has a negative effect on the performance of the cells [28, 42] (this is in contrast to CdTe cells, in which interdiffusion can actually improve performance [43]). Because of this, as well as the use of a TiO_2 barrier layer, both TiO_2 and ZnO have been investigated as emitter layers [38, 42, 45].

1.2.2   Deposition techniques

This project will focus on devices having antimony selenide layers deposited by thermal evaporation and close space sublimation. Hence these two techniques are outlined below.

Thermal Evaporation (TE)

Thermal evaporation is one of the oldest thin-film deposition techniques. A schematic of a typical TE setup is given in Figure 1.7. The source material is in the form of a solid target or a powder held in a crucible which is heated by either a coil of wire or an electron beam [46]. The material first melts and then evaporates [27]. The vapour then condenses and resolidifies on a substrate mounted above the source. The process is carried out under
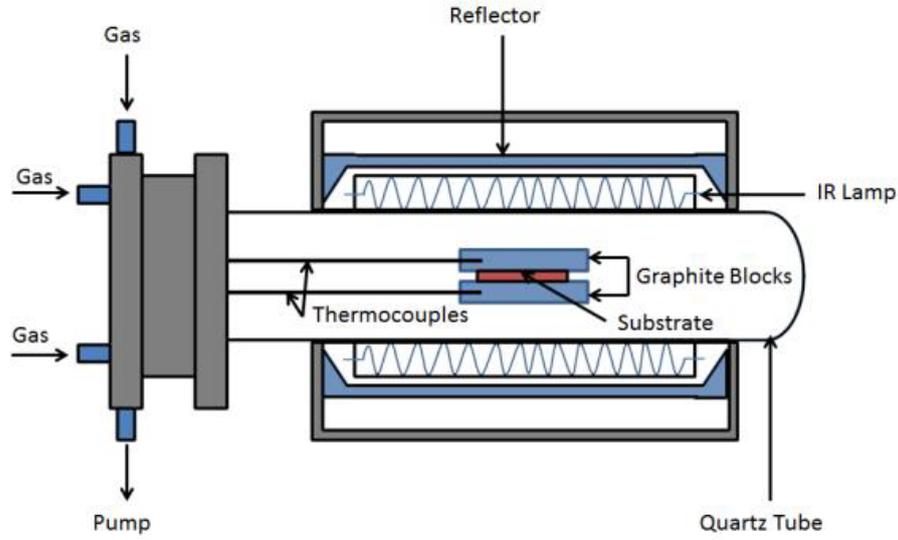
Figure 1.8: Schematic of a typical close space sublimation setup [50].

vacuum, in part to avoid atmospheric contamination of the deposited film [47].

The low pressure also affects the mean free path of the evaporated atoms or molecules. The mean free path, λ, for molecules in a gas is given by [47, 48]

$$\lambda = \frac{kT}{\sqrt{2}\pi P d^2} \tag{1.2.7}$$

where k is Boltzmann's constant, T is temperature, P is pressure, and d is the diameter of a gas molecule. From this it is clear that a low pressure will result in a large mean free path. This means that scattering of gas molecules will be minimal and they will travel rectilinearly from source to substrate [46].

A shutter is typically inserted between source and substrate to accurately control deposition time. In order to ensure an even film, the substrate may be rotated or heated [47]. For crystalline materials, heating the substrate will also affect the rate of nucleation of crystallites on the substrate, allowing grain size to be controlled [49]. TE is less well suited to the deposition of alloys, as some materials will evaporate at different rates to others, which will negatively impact the consistency of the film [46]. In rapid thermal exaporation (RTE) the distance between source and substrate is kept small in order to maximise deposition rate [27].

Close Space Sublimation (CSS)

Close space sublimation is a technique widely used in the growth of CdTe solar cells [29]. A source material is heated causing it to sublimate, in contrast to TE [27]. This vapour then reforms into a solid on the surface of a cooler substrate held above the source [48].

A typical CSS apparatus is shown in Figure 1.8. The process takes place in a glass or quartz tube containing two blocks of graphite; one holds the source in powder or solid form; the other holds the substrate. The substrate block is stacked on top of the source block with a spacer between them to set the source-substrate separation. The graphite blocks are heated by infra-red heating lamps, to which they are linked by thermocouples allowing precise control of their temperature. It is assumed that the temperatures of the source and substrate are equal to their respective blocks; however, because of the relatively small source-substrate distance (< 10 mm) this is not necessarily the case and the substrate is often heated above its target temperature [29, 38, 48].

In contrast to TE, CSS takes place in a pressurised gas environment (e.g. oxygen, nitrogen or argon) in order to help control the deposition rate. Because of this, the mean free path of the sublimated atoms is much lower than in thermal evaporation, necessitating the low source-substrate separation distance. This low separation means that it is often not possible to use a shutter to control deposition time. In order to prevent unwanted deposition before the source reaches its target temperature, the substrate is sometimes heated first [51, 52].

Despite this, CSS offers a number of advantages: its high deposition rate is comparable to RTE [27]; by varying the pressure and composition of the atmosphere grain size can be controlled [53]; and the source and substrate temperatures can be more accurately controlled than in TE [29]. For both CdTe and Sb_2Se_3, CSS has been shown to yield larger grains than TE, which allows for thicker, more absorbant films and reduces the impact of grain boundaries [38, 54].

One of the devices used in this project is grown by a novel two-stage CSS process. A short deposition is used to grow a compact seed layer, which is then annealed before a longer deposition is used to grow a thicker layer of Sb_2Se_3 on top of it. This is intended to improve the quality of the junction by increasing shunt resistance, and it is suggested that this may also improve grain orientation [45].

| Gold Back Contact |
| Sb$_2$Se$_3$ |
| CdS/TiO$_2$ |
| ZnO (optional) |
| TCO |
| Glass |

Figure 1.9: Schematic indicating the different layers of material in the devices used in this project.

1.3 Project Aims

The aim of this project is to combine focused-ion beam scanning electron microscopy (FIB SEM) milling with various transmission electron microscopy (TEM) techniques, including electron diffraction, high resolution electron microscopy (HREM), and energy dispersive x-ray spectroscopy (EDX) in order to analyse the effects of different growth techniques and emitter layer materials on Sb$_2$Se$_3$ solar cells. A schematic of the devices investigated is shown in Figure 1.9. Generally, the devices are in superstrate configuration, having a p-type Sb$_2$Se$_3$ absorber layer, and an n-type emitter layer made of either CdS or TiO$_2$.

The specifics for each device are as follows: sample A, Sb$_2$Se$_3$ grown by CSS on CdS with a ZnO buffer layer; sample B, Sb$_2$Se$_3$ grown by TE on CdS; sample C, Sb$_2$Se$_3$ grown by two-stage CSS on TiO$_2$; and sample D, a seed layer from the two-stage CSS process grown on TiO$_2$. The two growth techniques investigated are both commonly used, low-cost, and scalable for the production of thin-films, with TE being simpler, but CSS having numerous advantages as described in Section 1.2.2.

Performance parameters of samples A-C are shown in Table 1.1. While sample C shows the best performance, sample A has an extremely low efficiency largely due to decreased J_{SC}. This is despite XRD data indicating that both CSS cells have better orientation than the TE device. Secondary ion mass spectrometry (SIMS) data suggests high levels of interdiffusion between the CdS and Sb$_2$Se$_3$ layers of sample A, which may be responsible for the poor performance [38].

Sample	Description	η (%)	V_{OC} (V)	J_{SC}(mA cm^{-2})	FF (%)
A	CdS - CSS Sb$_2$Se$_3$	1.44	0.42	7.57	45.48
B	CdS - TE Sb$_2$Se$_3$	2.85	0.38	20.2	37.1
C	TiO$_2$ - CSS Sb$_2$Se$_3$	6.18	0.4	31.44	49.2
D	TiO$_2$ - CSS Sb$_2$Se$_3$ seed layer	-	-	-	-

Table 1.1: Descriptions and peak performance parameters of samples A-D. No performance parameters are given for sample D as it is not a complete device. Values obtained by Laurie Phillips, Peter Yates, Oliver Hutter, University of Liverpool [38, 55].

Although some scanning electron microscopy has been carried out to analyse morphology of the different devices, no TEM has yet been performed. TEM analysis can provide a range of information on the sample, including cross-sectional imaging showing grain boundaries to better understand device microstructure, electron diffraction and HREM to give information on the orientation of nanoribbons in individual grains, and EDX for high resolution mapping of interdiffusion.

Chapter 2

Electron Microscopy

2.1 Introduction

The resolution limit of the naked eye is approximately 0.1 mm. Using an optical microscope it is possible to achieve resolutions up to 200 nm. This limit arises from the fact that it is impossible to focus a beam of light to a perfect spot; rather it forms an Airy disc consisting of a bright central circle surrounded by concentric halos. The radius of the Airy disc is taken as the distance from the central maximum (the centre of this circle) to the first minimum. In order to be able to resolve two points, the distance between them must be greater than the radius of the Airy disc. This leads to Abbe's equation (first published by Ernst Abbe in 1873), which gives the maximum resolution d of a microscope as being

$$d = \frac{0.612\lambda}{n\sin(\alpha)} \tag{2.1.1}$$

where λ is the wavelength of light being used for imaging, n is the refractive index of the medium between source and lens, and α is the half aperture angle [56–58]. This shows the relationship between wavelength and resolution.

Later, in 1925, Louis De Broglie suggested that electrons (and all other matter) can behave as waves having a wavelength $\lambda = \frac{h}{p}$, where h is the Planck constant and p is the momentum of the particle. Taking into account relativity, for an electron accelerated across a voltage V, this equation becomes

$$\lambda = \frac{h}{\sqrt{2eVm_e + \frac{e^2V^2}{c^2}}} \tag{2.1.2}$$

where m_e and e are the rest mass and charge, respectively, of an electron, and c

is the speed of light [57, 58]. For an electron accelerated across 200 kV (the standard operating voltage of a transmission electron microscope) this gives $\lambda = 0.0025$ nm, which is 10^5 times smaller than the wavelength of visible light [58]. De Broglie's hypothesis and Abbe's equation together demonstrate that with an electron microscope it is possible to achieve resolutions far superior to those available using an optical microscope, allowing the microstructure of thin-films to be imaged with good detail.

The first transmission electron microscopes (TEM) were constructed in the 1930s. These operate in a way analagous to an optical microscope, but with electromagnetic lenses used to focus a beam of electrons onto a sample. The electrons which are transmitted through the sample are focused onto a phosphor screen or a CCD to form an image [56, 57].

The first scanning electron microscope (SEM) was constructed not long after. In an SEM, a focused beam of electrons is rastered over a sample and the various signals given off can be detected and used to form an image [56, 57].

2.1.1 Electron Guns

In both TEM and SEM systems, the electron beam is produced by either a thermionic emission gun, or a field emission gun (FEG). In the simplest thermionic emission system a v-shaped tungsten filament is used as the cathode. This is heated to over 2800 K, which gives the electrons in the material enough energy to overcome the work function, leading to their emission from the source. As the cathode is negatively biased relative to an earthed anode, the electrons flow from cathode to anode. Between the anode and the cathode is a Wehnelt cylinder, which is negatively biased relative to the cathode, and which focuses the electrons into a beam. An alternative thermionic emission system utilises a LaB_6 crystal in place of the tungsten filament. This is held in a graphite mount which is heated, passively heating the crystal. This system offers many advantages over the tungsten filament: as LaB_6 has lower work function, it emits more electrons at lower temperatures and provides greater brightness; it also allows a smaller spot with less energy spread, leading to better resolution [56, 57, 59].

A field emission gun uses a single crystal tungsten source with a fine tip. When a voltage is applied between an extraction anode and the source a very strong electric field forms at the tip. This lowers the vacuum energy level relative to the Fermi energy of the tip, allowing electrons to escape via tunelling. Field emission sources are much brighter than thermionic emission sources and provide a smaller spot size and less energy spread,
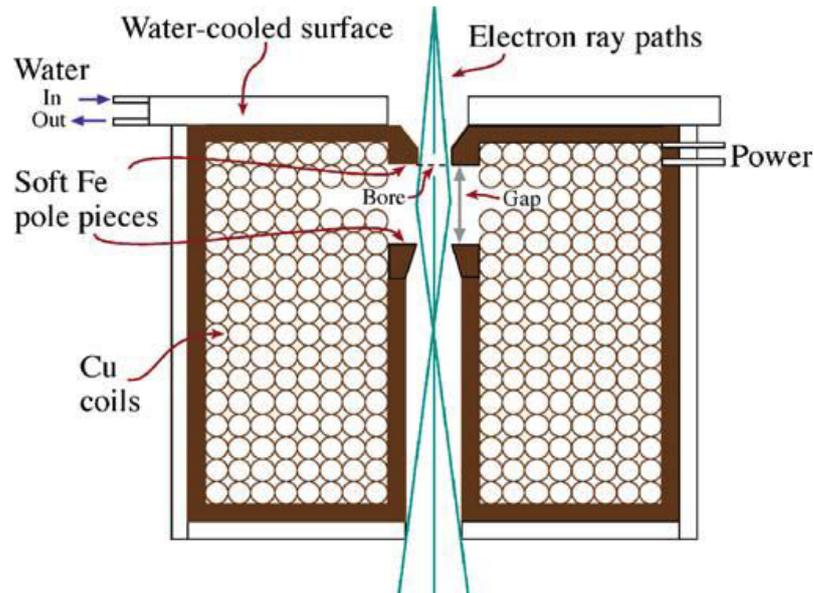
Figure 2.1: Schematic diagram of an electromagnetic lens, in which the two pole pieces are part of the same piece of iron. [57].

however the beam current is lower overall [56, 57, 59].

2.1.2   Electron Lenses

In an electron microscope, electromagnetic lenses are used to focus the beam. When a charged particle such as an electron passes through a magnetic field it experiences a force proportional to the cross-product of its velocity vector and the magnetic field vector. Therefore an electron travelling parallel to the field would experience no force. A diagram of an electromagnetic lens is shown in Figure 2.1. This consists of two hollow cylindrical pole pieces, which may be either a single piece of iron or two separate pieces, with copper windings. These produce an electric field parallel to the optic axis down the centre of the pole pieces [56, 57]. Therefore an electron travelling straight down the optic axis will be unaffected, however one that is not parallel to this will experience a force causing it to travel along a helical path to converge with the parallel beam [58, 59].

2.2   Scanning Electron Microscopy (SEM)

In SEM, a narrow convergent beam of electrons is scanned over a sample at typical beam energies of 5-20 kV. After being emitted from the electron gun, the beam is demagnified by the condenser lens and will pass through an aperture to limit the beam diameter and
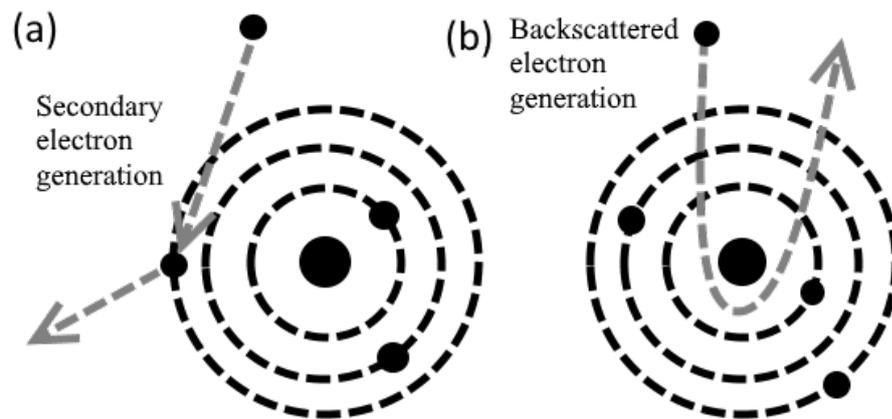
Figure 2.2:   Diagram showing the processes by which secondary electrons (a), and backscattered electrons (b) are emitted.

current, before being focused into a 'point' on the sample surface by the objective lens [58]. Stigmation poles are used to adjust the beam profile and ensure it is circular rather than elliptical, and scanning coils are used to deflect the beam and raster it over the sample [56]. The electrons interact elastically and inelastically with the sample to produce a variety of signals including secondary electrons, backscattered electrons, characteristic X-rays and cathodoluminescence. The resolution of SEM imaging is limited by the area from which signals are emitted. This is linked to both the diameter of the probe at the specimen surface, and the interaction of the electrons with the specimen [56, 58].

Secondary electrons are the most widely used for imaging. These are produced from inelastic scattering of incident electrons, causing loosely bound atomic electrons to be emitted from the sample, as illustrated in Figure 2.2 (a). These electrons are low energy (below 50 eV) and are therefore emitted from within a few nm of the sample surface. Secondary electron imaging provides information on the topography of a sample through both shadowing (topographic features blocking emitted electrons from reaching the detector), and also through the dependence of secondary electron emission on the electron beam angle of incidence on the sample (if the beam is perpendicular to the surface of the sample, electrons are emitted from a smaller volume than if the beam is at an angle, as is shown in Figure 2.3 [56]). The effect of this is illustrated in Figure 2.4; the sides of the grains appear bright in the image due to increased secondary electron emission.

Backscattered electrons are incident electrons which undergo elastic scattering by large angles, as illustrated in Figure 2.2 (b). They have higher energies, and are typically emitted from deeper within the sample than secondary electrons. Elements with higher
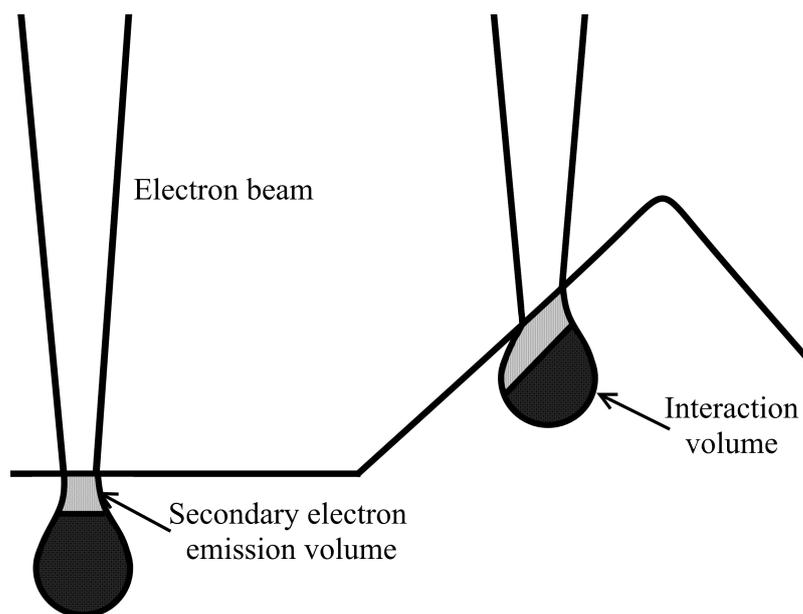
Figure 2.3:   Diagram showing how the secondary electron emission volume varies with topography.
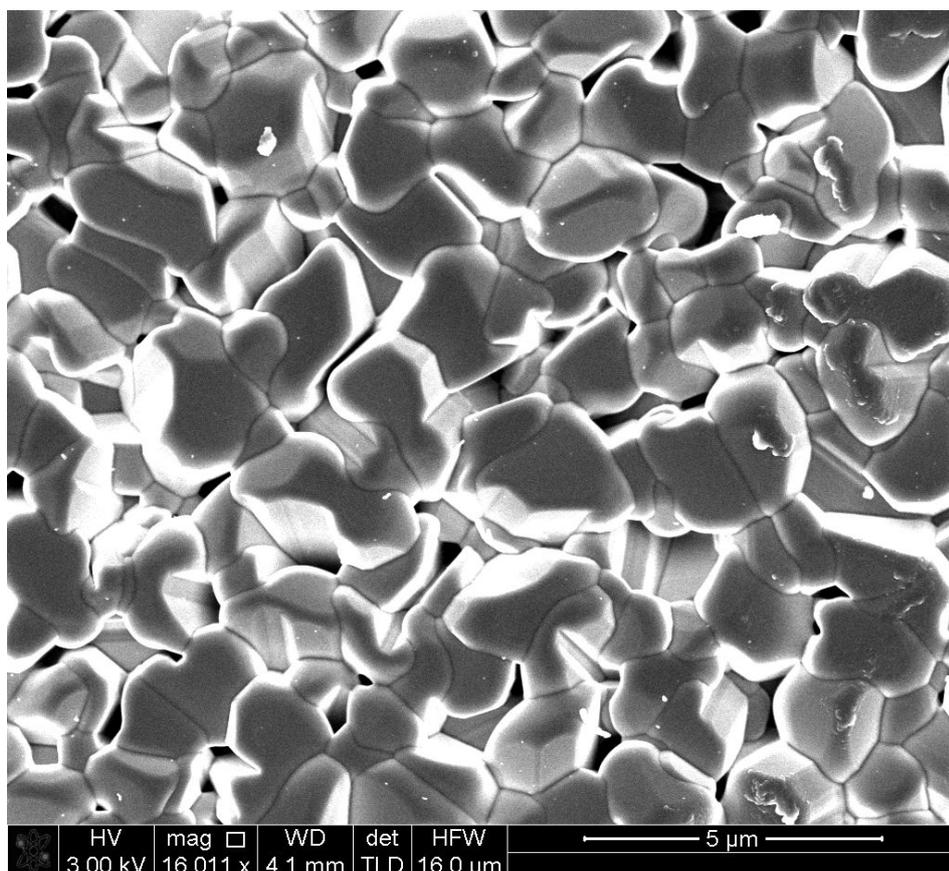
Figure 2.4: Top down image of an Sb_2Se_3 thin-film showing topographic contrast.
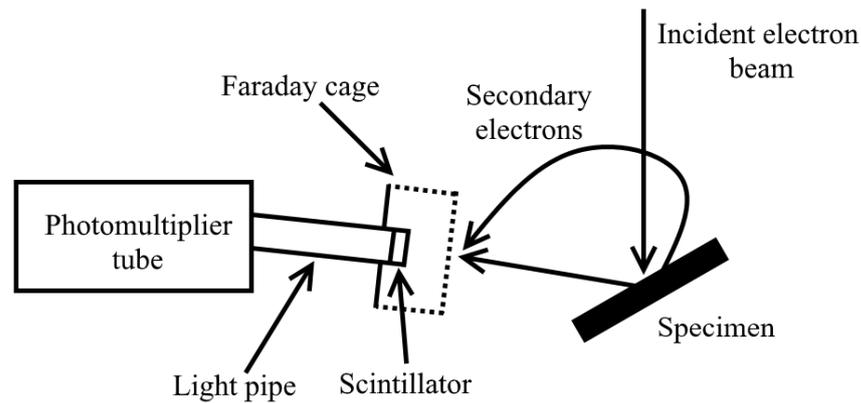
Figure 2.5: Schematic diagram of an Everhart-Thornley detector.

atomic numbers backscatter more electrons than those with smaller nuclei, so imaging using backscattered electrons provides chemical contrast [56, 58].

Secondary and backscattered electrons are detected using an Everhart-Thornley detector, a diagram of which is shown in Figure 2.5. This consists of a scintillator which is biased to 10 kV, which causes the secondary electrons travelling towards it to gain enough energy to cause the emission of photons. Backscattered electrons have high enough energy to excite the detector without further acceleration. These photons are transmitted through a light pipe to a photomultiplier tube which converts the photons into an electrical current, the strength of which corresponds to the measured signal from the point on the sample surface at which the electron beam is incident. To avoid the electric field of the scintillator disrupting the electron beam, it is shielded by a Faraday cage. This is weakly biased in order to attract low energy secondary electrons which may not have been moving towards the detector, but does not affect the higher energy beam electrons (5-30 keV) [56, 59].

2.3 Focused Ion Beam Scanning Electron Microscopy (FIB SEM)

A FIB SEM combines a scanning electron microscope (SEM) and focused ion beam microscope (FIB). As shown in Figure 2.6, in a FIB SEM the electron beam and ion beam are at 52° to one another. The sample is mounted on a stage having translation, rotation and tilting capabilites, and the system is designed to have a eucentric point, i.e. a point at the centre of the ion and electron beam images which is unchanged by tilting. The FIB SEM has imaging, milling and deposition capabilities [60].
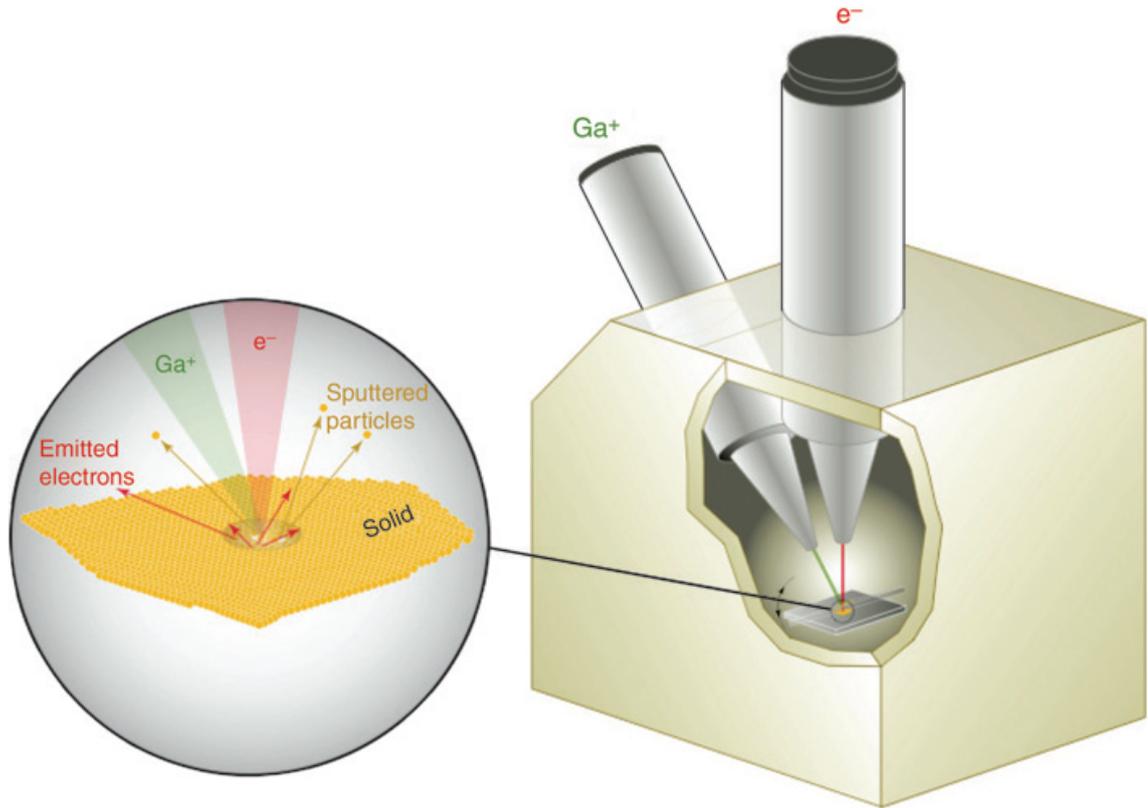
Figure 2.6: Illustration of a FIB SEM [60].

A focused ion beam microscope (FIB) works along the same principles as the SEM. The electron beam is replaced with a beam of ions, usually gallium, produced by a liquid metal ion source (LMIS). This consists of a reservoir of liquid metal and a tungsten needle. The liquid metal flows to the tip of the needle, where it forms a cone with a tip of around 5 nm. As in a FEG, a strong electric field (10^{10} V m^{-1}) around the tip causes the emission of metal ions, which flow towards an extraction electrode which is negatively biased with respect to the needle tip. As in the SEM, the ions pass through lenses, apertures, stigmators and scanning plates [60].

A key difference in an ion beam system is the use of electrostatic rather than electromagnetic lenses. Ions are relatively massive and slow moving compared to electrons. Because of their large momentum the force required to deflect them is much greater than that needed by an electron, but the force applied by a magnetic field is proportional to velocity, so impractically large magnetic fields would be needed to focus the ion beam. A typical electrostatic lens, as shown in Figure 2.7, consists of three electrodes parallel to the beam direction. Large potential differences between the electrodes generate electric fields which divert the ions towards the beam axis [61].
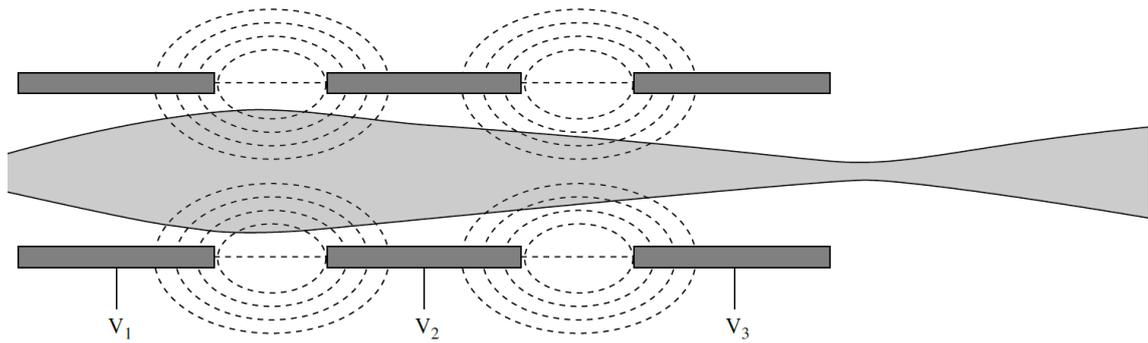
Figure 2.7: Diagram of an electrostatic lens [61].

When the ion strikes the sample it undergoes a series of elastic and inelastic collisions. The inelastic interactions are similar to those in the SEM; the ion transfers energy to electrons leading to the emission of low energy ion-induced secondary electrons and X-rays, which can be used for imaging and chemical analyis. Ion beams are more poorly focused and have a larger spot size than electron beams leading to a worse resolution [60].

Because of the high kinetic energy of the ions, in inelastic collisions energy is transferred to atoms which can lead to sample damage or sputtering. When an atom gains kinetic energy and is knocked out of its site, it may interact inelastically with further atoms in the sample leading to a disordered volume of the sample. If this takes place close to the surface, atoms may escape from the sample leading to sputtering. Other forms of damage include amorphisation, and the formation of point defects and dislocations. The gallium ions will come to rest inside the sample, causing gallium implantation [60].

The sputtering effect means that the FIB can be used to mill patterns with a precision matching the resolution of the instrument. The rate of milling and the exact pattern produced are complex, depending on redeposition, material density, grain orientation and beam angle; however, it can be computer controlled to allow the milling of relatively complicated patterns. A FIB or FIB SEM also has chemical vapour deposition capabilities: the secondary electrons produced by the ion or electron beam cause a precursor gas to decompose, leading to the deposition of material. [60, 61]

These capabilities allow the FIB SEM to be used for a range of applications in sample preparation and analysis, including cross-sectional imaging and the fabrication of TEM samples.

2.4 Transmission Electron Microscopy (TEM)

In TEM, a high energy beam of electrons (typically 200 kV accelerating voltage) is transmitted through the sample. In order to maximise the number of electrons which pass through the sample and obtain a detailed image, the sample must be made as thin as possible. In a TEM, the beam of electrons emitted by the electron gun is directed onto the sample by two condenser lenses. In contrast to SEM where the beam must be focused on the sample, in TEM the beam diameter over which the sample is illuminated can be varied through the condenser lenses. The TEM is often operated in parallel illumination mode, where a large region of the specimen is illuminated by parallel electron "rays". After passing through the sample, the objective lens focuses the transmitted electrons into an intermediate image and diffraction pattern, as shown in Figure 2.8, and a series of projector lenses is then used to magnify and project whichever of these is being viewed onto either a screen coated with a material such as ZnS, which emits visible light when excited by electrons, or onto a CCD which allows the image to be recorded and viewed on a computer [57].

There are three primary contrast mechanisms in the TEM, namely mass-thickness contrast, diffraction contrast, and phase contrast. Mass-thickness contrast arises from the fact that electrons will interact with and undergo more scattering in areas of the sample that are thicker or composed of elements with a higher atomic number, than by areas which are thinner or less dense [57, 58].

Diffraction contrast arises from the Bragg scattering of electrons in a crystalline sample. By inserting an aperture in the objective lens back focal plane (shown in Figure 2.8), it is possible to form an image using electrons which have been scattered from a particular crystal plane; in the resultant image, crystals which are oriented such that the plane is in the Bragg condition will appear brighter. This is known as a dark-field image. Alternatively, by using an aperture to select only the unscattered beam, crystals which are close to the Bragg condition scatter electrons more strongly and will therefore appear darker. This is known as a bright-field image. Mass-thickness contrast is also increased in a bright-field image [57, 58].

When electrons interact with the sample they inevitably undergo phase changes. Phase contrast arises from the interaction bewteen electron beams with different phases, and is used for imaging the crystal lattice (section 2.4.2) [57, 58].

Referring back to section 2.1, by substituting the wavelength of a 200 keV electron
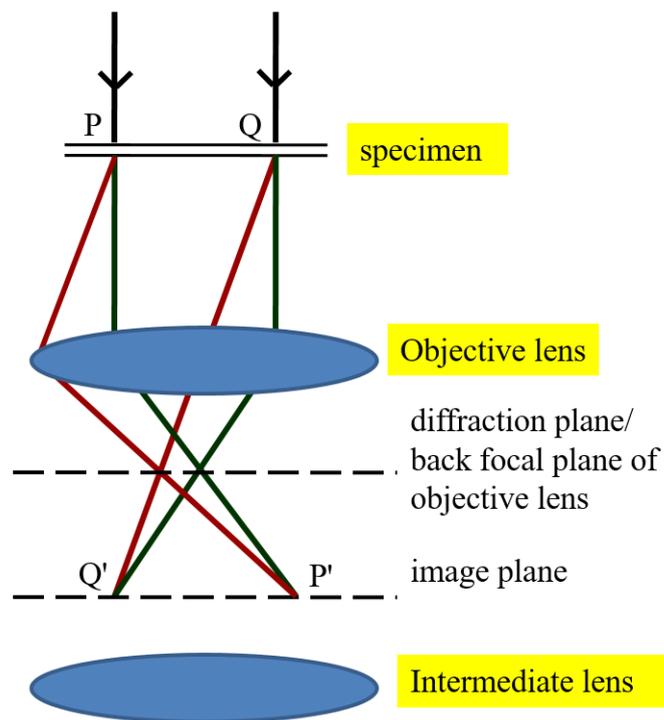
Figure 2.8: TEM ray diagram, showing the formation of both the image and the diffraction pattern.

into Abbe's equation, a maximum theoretical resolution limit for the TEM is found to be around 0.01 nm. This is much smaller than an atom. Unfortunately it is impossible to obtain this resolution in a TEM due to lens aberrations. There are several sources of aberration in an electron microscope [58]. The first is stigmation; as in SEM this is caused by asymmetric focusing of the beam by the lens, and is corrected using stigmators. The next source of aberration is chromatic aberration. Generally the beam produced by the electron gun has a low energy spread; however electrons will lose energy when interacting with the sample so that the transmitted electrons will have a higher energy spread. This is limited by making the sample thinner. The ultimate limiting factor in the resolution of a TEM is spherical aberration. This is where the lens refracts off-axis beams more strongly than on-axis beams, causing a point to be imaged as a disc [57].

In a TEM, the diffraction pattern is formed at the back focal plane of the ojective lens. This is the plane at which all beams scattered in the same direction, regardless of specimen position, are focused into a single point, as illustrated in Figure 2.8. To view a diffraction pattern the intermediate lens uses the objective back focal plane as the object. In order to obtain a diffraction pattern from a specific area in a sample, such as a crystal

grain, a selected area aperture is inserted into the image plane of one of the lenses following the objective lens. This blocks out all electrons not originating from that region in the sample [57–59]. The mechanism by which diffraction patterns form is outlined in section 2.4.1.

2.4.1 Electron Diffraction

Electrons scattering off atoms in a crystal can interfere with one another to produce diffraction, similar to that observed by light passing through a diffraction grating. The diffraction of electrons by a set of crystal planes (hkl) is described by Bragg's law [57–59]:

$$n\lambda = 2d_{hkl}\sin\theta \tag{2.4.3}$$

where n is the order of diffraction, λ is the electron wavelength, d is the separation of the planes (hkl), and θ is the angle of incidence of the electrons on the crystal plane. As the wavelength of electrons is very small, the Bragg angle θ is also small, to the point that the crystal plane can be considered to be effectively parallel to the electron beam in order for diffraction to take place [58]. If the crystal is oriented such that the beam is along a zone axis (i.e. a specific crystallographic direction such as [100], [110] etc.), a diffraction pattern consisting of a regular array of spots is produced, with each spot corresponding to a set of planes parallel to the electron beam [57–59].

A crystal lattice in real space defined by vectors $\mathbf{a}$, $\mathbf{b}$, $\mathbf{c}$, has a corresponding reciprocal lattice defined by vectors $\mathbf{a^*}$, $\mathbf{b^*}$, $\mathbf{c^*}$ [57], where

$$\mathbf{a^*} = \frac{\mathbf{b}\times\mathbf{c}}{\mathbf{a}\cdot(\mathbf{b}\times\mathbf{c})} \qquad \mathbf{b^*} = \frac{\mathbf{c}\times\mathbf{a}}{\mathbf{a}\cdot(\mathbf{b}\times\mathbf{c})} \qquad \mathbf{c^*} = \frac{\mathbf{a}\times\mathbf{b}}{\mathbf{a}\cdot(\mathbf{b}\times\mathbf{c})} \tag{2.4.4}$$

For a system where $\mathbf{a}$, $\mathbf{b}$, $\mathbf{c}$ are orthogonal to one another, the result of this is that $\mathbf{a^*}$ is parallel to $\mathbf{a}$ and has a length equal to the reciprocal of $\mathbf{a}$. $\mathbf{b^*}$ and $\mathbf{c^*}$ are similarly related to $\mathbf{b}$ and $\mathbf{c}$ [62].

The reciprocal lattice and the diffraction pattern are related by the Ewald sphere. The construction of this is shown in Figure 2.9; a line is drawn of length $\frac{1}{\lambda}$ along the beam direction from C and terminating at the origin O of the reciprocal lattice. If a sphere of radius $\frac{1}{\lambda}$ is then drawn around C, any point in the reciprocal lattice that this sphere passes through will correspond to a set of planes which satisfy Bragg's law for that particular beam direction, with point O corresponding to the unscattered beam [57–59].
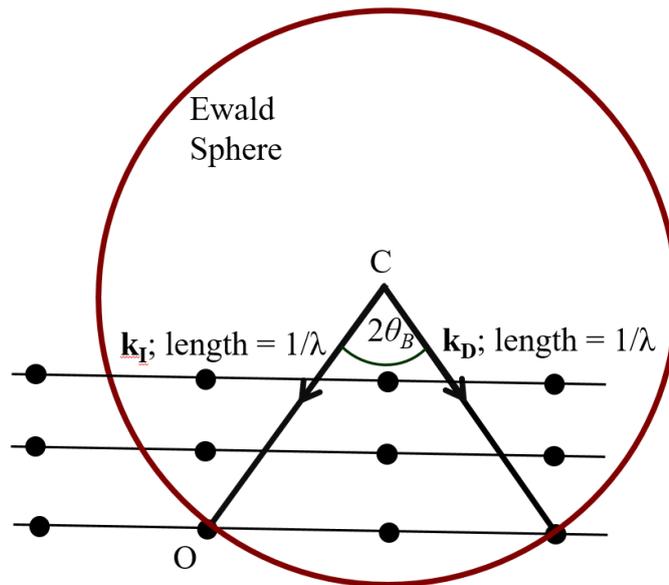
Figure 2.9: Diagram illustrating the Ewald sphere. $\mathbf{k}_I$ is the incident beam vector, $\mathbf{k}_D$ is the diffracted beam vector [57].

2.4.2   High Resolution Electron Microscopy (HREM)

It is possible to image the crystal lattice in the TEM using phase contrast arising from interference between scattered and unscattered electron beams. Because of this it is necessary to use a larger objective aperture, unlike diffraction contrast and mass-thickness contrast images, to allow both the scattered and unscattered beams to contribute to the image. The crystal lattice acts similarly to a diffraction grating, where the constructive and destructive interference leads to intensity maxima and minima, which form an image of the lattice.

For a thin sample oriented such that the beam is directed along a zone axis, at an optimum defocus, the image formed can be intuitively interpreted as dark spots representing lattice points. In some cases these dark spots correspond to individual columns of atoms, however due to limitations in resolution these spots may instead correspond to groups of atoms. For instance in an image of a [110] oriented silicon lattice the dark spots may correspond to columns of atom pairs [59, 63].

For thicker samples and different defocus values, variation in the intensities and phases of the transmitted and scattered beams can lead to the contrast in the image being reversed. Nonetheless, in almost all cases the pattern of spots will still correspond to the periodicity and orientation of the crystal lattice, even if it is unclear whether atom
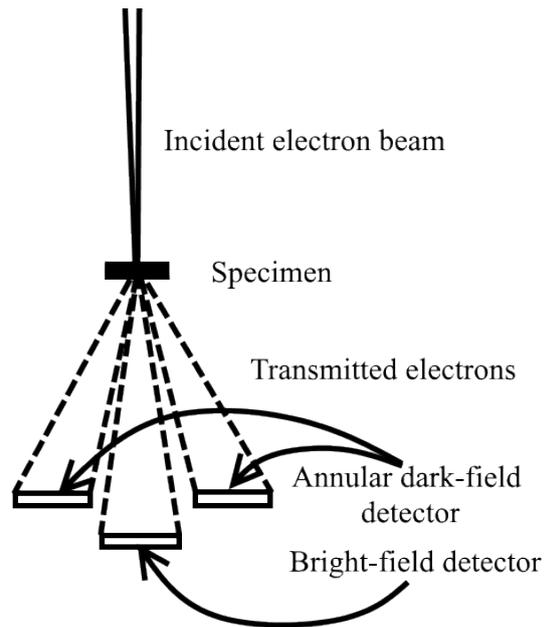
Figure 2.10: Diagram illustrating the bright-field and annular dark field detectors in a STEM.

columns correspond to intensity minima or maxima [57, 59, 63].

2.4.3 Scanning Transmission Electron Microscopy (STEM)

STEM has similarities to both SEM and TEM, in that a focused electron beam is scanned over the sample and an image is formed from the transmitted electrons [58, 59]. As in TEM, bright field and dark field images can be formed from the transmitted and scattered electrons respectively; however, this is acheived through the use of specialised detectors rather than apertures, as shown in Figure 2.10. The bright field detector takes the form of a scintillator disc which detects the unscattered electrons and some of those scattered by small angles. The dark field detector is an annular detector and takes the form of an annulus which detects those electrons scattered out to large angles. The transmitted electrons can pass through the hole in the centre of the annular detector to reach a bright field detector underneath. This allows both images to be viewed simultaneously [57, 64].

If the hole of the annular detector is very large the resulting images are known as high angle annular dark field (HAADF). The electrons detected to form a HAADF image have undergone Rutherford scattering in order to be deflected by high angles. Because the probability of an electron undergoing Rutherford scattering is proportional to Z^2, where Z is the atomic number of the nuclei in the sample, heavier elements appear brighter than

lighter ones. Through this method it is possible to obtain high resolution images showing individual atoms, the chemical identity of which can be determined by their intensity in the HAADF image. This allows accurate imaging of the crystal lattice and defects [64].

2.4.4 Energy Dispersive X-ray Spectroscopy (EDX)

When an electron interacts with the sample, X-rays are produced which can be detected and recorded to form a spectrum which gives chemcial information on the sample. There are two processes through which X-rays are produced. In the first incident electrons interact inelastically with inner shell electrons in the sample, causing them to be excited to a higher energy level or to escape the atom. When a higher energy electron relaxes to fill the gap in the lower shell, it releases the excess energy in the form of an X-ray. These are known as characteristic X-rays, and give rise to discrete peaks in the spectrum, the energy of which is indicative of the element from which they were released. The second source of X-rays is bremsstrahlung radiation. This is radiation given off by beam electrons when they change momentum during scattering interactions with atomic nuclei. This forms a continuous background on the spectrum [65].

The X-rays are detected using a silicon drift detector. In this, a voltage is applied to a silicon crystal. When an X-ray strikes the silicon it creates electron-hole pairs which allow a pulse of current to flow through the crystal. The size of this current is proportional to the X-ray energy, allowing the energy of the X-ray which caused the current to be measured [65].

When used with a scanning or scanning transmission electron microscope, EDX data can be used to create maps or linescans showing the distribution of different elements in a sample [64]. The thin specimen used in STEM allows higher resolution mapping than a thicker SEM sample would, due to the smaller electron beam interaction volume for STEM [65]. The thinner sample does however lead to a significantly weaker X-ray signal, since most of the high energy electrons are transmitted through the sample without inner shell ionisation. Because of this STEM EDX mapping is done at lower spatial resolutions compared to STEM imaging so that a higher beam current can be used and hence a stronger X-ray signal obtained [64, 65].

Chapter 3

Experimental Procedure

3.1 Material Deposition

The samples analysed in this project were deposited by Laurie Phillips, Peter Yates, and
Oliver Hutter at the University of Liverpool. The samples were grown in superstrate
configuration according to the schematic given in Chapter 1, Section 1.3 (Figure 1.9). All
were grown on fluorine doped tin oxide (FTO) coated glass substrates (TEC10 supplied
by NSG Ltd.). Close space sublimation was carried out using a system custom-built
by Electro-Gas Systems, Ltd. Thermal evaporation was carried out using a Moorfields
multi-source evaporation chamber. A summary of all samples is given in table 3.1.

3.1.1 Sample A

Sample A consists of a layer of antimony selenide deposited on a cadmium sulfide emitter
layer by close space sublimation, with a zinc oxide buffer layer between the CdS and
the transparent conducting oxide (TCO) layer. The CdS and ZnO were both deposited
by sputtering; the ZnO at 150 W for 50 mins at room temperature, and the CdS at

Sample	Description
A	CSS Sb_2Se_3 on CdS
B	TE Sb_2Se_3 on CdS
C	CSS Sb_2Se_3 on TiO_2
D	Seed layer

Table 3.1: Summary of samples.

60 W for 15 mins with the susbtrate at 200°C, without breaking vacuum between the two depositions.

For the CSS deposition of Sb_2Se_3, the source-substrate distance was approximately 5 mm. The source was first heated to 360°C and the substrate to 390°C under vacuum and held for 5 minutes. The source was then heated to 470°C under 13 mbar N_2. After 10 minutes deposition at 470°C, pressure was increased to 400 mbar and heating was switched off to halt deposition. Although the target substrate temperature during deposition was only 390°C, the substrate would have reached over 400°C due to heating from the source block.

3.1.2   Sample B

The Sb_2Se_3 layer in sample B was deposited by thermal evaporation on a CdS emitter layer, again deposited by sputtering. The thermally evaporated material was deposited at room temperature under vacuum with a source-substrate separation of 20 cm, prior to annealing in a glove box under N_2 at 350°C for 30 minutes [55].

3.1.3   Sample C

Sample C was deposited on a TiO_2 emitter layer by a two stage CSS process. The substrate was spin coated with 0.15 M and 0.3 M titatium isopropoxide at 3000 rpm for 30 s, and dried at 120°C in N_2 after each deposition. It was then annealed in air at 550°C to form the TiO_2 layer.

For the two stage CSS process, first a seed layer was grown by heating the source to 350°C and the substrate to 380°C under 0.05 mbar N_2 for 5 minutes. This layer was then annealed in 260 mbar N_2 for 10 minutes while remaining at 380°C. The second stage of CSS was then carried out for 30 minutes at a source temperature of 450°C under 13 mbar pressure, before the substrate was cooled with N_2 to halt deposition. Although the substrate was not directly heated during the second stage of deposition, it would still have reached over 400 °C due to heating from the source block [45].

3.1.4   Sample D

Sample D is a seed layer grown on TiO_2. This was grown using the first stage of the CSS process used to grow sample C, as outlined in section 3.1.3 [45].

3.2   Electron Microscopy

3.2.1   FIB SEM

An FEI Helios Nanolab DualBeam system was used both for top down and cross-sectional imaging of the devices, and also to prepare cross-sections for analysis in the TEM. This has a Shottky-type FEG as an electron source. This is a thermally assisted field emission gun, in which the tungsten tip is coated with ZrO_2 to improve emission. This is capable of a range of accelerating voltages from 200 V-30 kV, and a range of beam currents from 0.7 pA to 22 nA, enabling an optimum electron beam size of around 1 nm. The ion beam uses gallium ions emitted from a liquid metal ion source. This is capable of a range of accelerating voltages from 500 V to 30 kV, and a range of beam currents from 0.1 pA to 6.5 nA, enabling an ion beam size of around 4 nm. The microscope has a standard Everhart-Thornley detector for secondary and backscattered electron imaging, as well as an in-lens secondary electron detector. The in-lens secondary electron detector was used for SEM imaging in this project.

To aid sample preparation, the microscope is fitted with a gas injection system to allow chemical vapour deposition of platinum, and an OmniProbe needle for lifting out TEM samples. The preparation of TEM samples using the FIB SEM is described below.

TEM sample preparation using FIB SEM

To begin the electron beam is used to deposit a thin layer of platinum over the region of the sample to be used for the cross-section. This is to protect the sample from ion beam damage. The stage is then tilted by 52° so that the surface of the cell is normal to the ion beam and the ion beam is used to deposit a layer of Pt around 3 µm thick.

Next, the ion beam at 30kV is used to mill a trench on each side of the platinum layer. As the Sb_2Se_3 layers in the cells analysed could be up to 4 µm thick, the trench needed to be over 6 µm deep to ensure that the device could be undercut with a layer of glass 2-3 µm thick below it. At this stage the SEM can be used to obtain cross-sectional images of the device.

Next the stage is returned to 0° tilt and the ion beam is used to undercut the sample. The stage is rotated by 180° and the cut repeated from the opposite side to ensure the cut goes all the way through the cross-section. The Omniprobe needle is inserted and the ion beam is used to deposit a layer of platinum attatching it to the layer of Pt above the
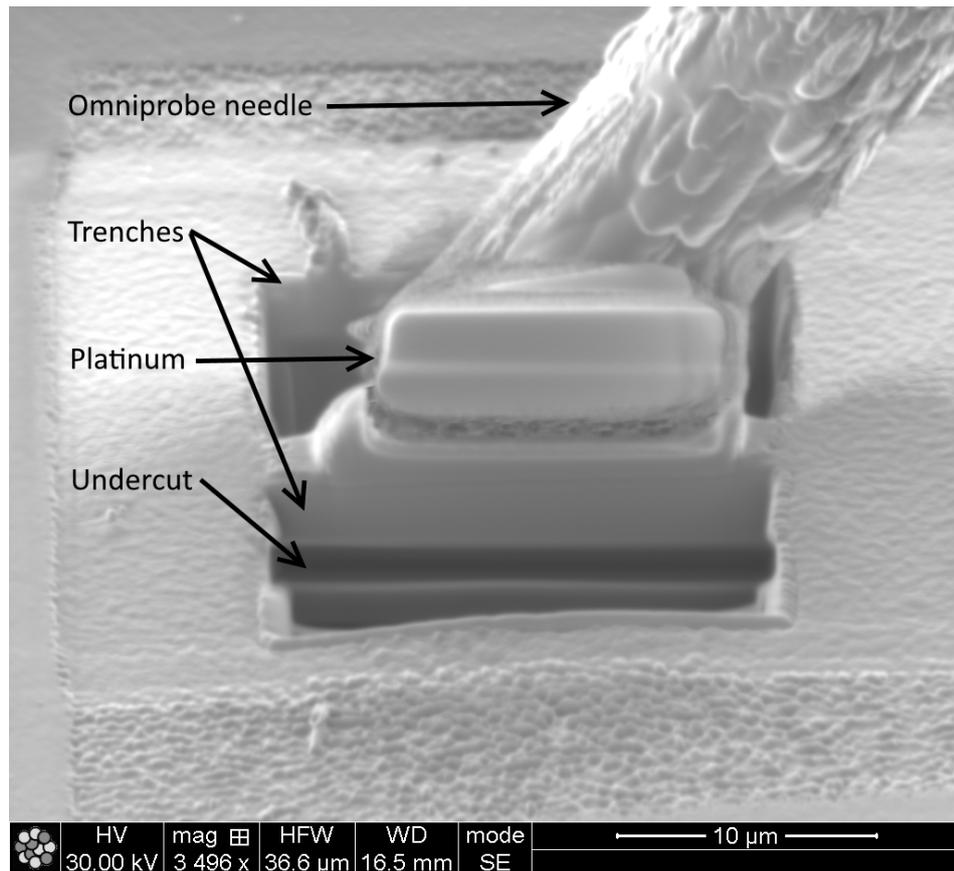
Figure 3.1: Ion beam image illustrating the TEM sample preparation process. The ominprobe needle is shown attatched to the ion beam platinum layer. Trenches and undercut are also visible.

cross-section. The process up to this point is illustrated in Figure 3.1. Following this, the ion beam is used to cut away the sides of the cross-section so that it can be lifted out of the device.

Ion beam platinum deposition is then used to attatch the cross-section to an Omniprobe sample grid. The ion beam is used to cut the cross-section free of the needle before the stage is tilted to 54° for coarse thinning of the sample at 16 kV. The thinning is carried out at 54° to ensure the bottom of the sample (i.e. the glass, FTO and emitter layer) are adequately thinned [66]. The stage is rotated by 180° to thin the sample from the opposite face. Thinning at 16 kV is continued until the cross-section reaches around 1 µm thick. As thinning progresses, the width of the area milled should be reduced, giving the sample a stepped profile; this increases the mechanical strength of the approximately 100 nm thick final sample.

After the 16 kV thinning is completed, the stage is tilted to -9 ° and the ion beam

is used to cut the sample down to a rectangular cross-section. This helps to ensure the subsequent thinning is uniform. The stage is then returned to 54° and thinning is resumed at 8 kV. Thinning continues at progressively lower voltages, down to 5 kV. The stage is rotated by 180° after each pass so that thinning on each side can be monitored using the electron beam. After 5 kV thinning, the platinum layer should be nearly exhausted, and the cross-section should appear bright in the electron beam image, indicating electron transparency.

3.2.2   TEM

TEM, STEM and EDX data were obtained using a JEOL 2100F Field Emission Microscope. This also uses a Schottky-type field emission gun to generate an electron beam. All work was carried out at an accelerating voltage of 200 kV. A double tilting specimen holder was used to tilt crystal grains to zone axis to allow diffraction patterns and high resolution lattice images to be obtained. The microscope is capable of of operating at magnifications of up to 1,500,000× and has a point resolution of 0.23 nm. The microscope can be operated in STEM mode, and is fitted with an Oxford Instruments X-max 65T silicon drift detector for EDX analysis.

The electron diffraction patterns were used to estimate the orientations of the Sb_2Se_3 ribbons relative to the surface normal of the emitter layer (i.e. film thickness direction). To do this the diffraction patterns of the Sb_2Se_3 grains were indexed and compared to a conventional TEM image of the interface between the Sb_2Se_3 and emitter layer, allowing the interface plane to be expressed in terms of reciprocal lattice vectors. This was then converted into a cartesian vector in real space, and the angle between this vector and the 001 ribbon direction was calculated. Further details are outlined below.

Indexing diffraction patterns

This section describes the process of indexing diffraction patterns for orthorhombic materials such as Sb_2Se_3. The first stage is to calculate the magnitude of the reciprocal lattice vectors for the low order sets of planes in the material being investigated. For a set of planes (hkl), the spacing between them d_{hkl} is given by

$$d_{hkl} = \frac{1}{\sqrt{\left(\frac{h}{a}\right)^2 + \left(\frac{k}{b}\right)^2 + \left(\frac{l}{c}\right)^2}} \tag{3.2.1}$$

where a, b and c are the unit cell dimensions. The magnitude of the reciprocal lattice

vector hkl* is then given by

$$\frac{1}{d_{hkl}} = \sqrt{\left(\frac{h}{a}\right)^2 + \left(\frac{k}{b}\right)^2 + \left(\frac{l}{c}\right)^2} \tag{3.2.2}$$

and the angle between two reciprocal lattice vectors $h_1 k_1 l_1$* and $h_2 k_2 l_2$* is ϕ, where

$$\cos\phi = \frac{h_1 h_2 + k_1 k_2 + l_1 l_2}{(h_1^2 + k_1^2 + l_1^2)^{\frac{1}{2}} (h_2^2 + k_2^2 + l_2^2)^{\frac{1}{2}}} \tag{3.2.3}$$

To index a diffraction pattern, the two smallest vectors and the angle between them are measured and then compared to calculated values to find which reflections they most likely correspond to. The cross product of these vectors then gives the beam direction, which by convention is calculated as coming out of the page [57, 59].

To check that the pattern has been indexed correctly, a diffraction pattern is constructed from the two vectors normal to the beam direction with the smallest values of $\frac{1}{d_{hkl}}$. This should correspond to the indexed pattern.

Finding the angle between the normal to the substrate and the Sb$_2$Se$_3$ ribbons.

This section describes how the diffraction pattern from an Sb$_2$Se$_3$ grain is used to find the angle between the normal to the substrate and the normal to the (001) planes (the latter corresponding to the Sb$_2$Se$_3$ ribbon direction). Using a conventional TEM image showing the interface between the Sb$_2$Se$_3$ and the emitter layer, as illustrated in Figure 3.2, the normal to this interface is traced onto the diffraction pattern, and expressed as a sum of Sb$_2$Se$_3$ reciprocal lattice vectors.

Taking one reciprocal lattice vector to be **x*** and another to be **y***, a vector **y'*** is then drawn perpendicular to **x*** (Figure 3.2). Taking **x*** and **y*** as basis vectors, a unit vector, **n̂***, parallel to the substrate normal (i.e. film thickness direction) can be expressed as

$$\hat{\mathbf{n}}^* = a\mathbf{x}^* + b\mathbf{y}^*$$

where a and b are given by

$$a = \frac{1}{|\mathbf{x}^*|}(\sin\beta - \cos\beta\tan\alpha) \qquad b = \frac{1}{|\mathbf{y}^*|}\frac{\cos\beta}{\cos\alpha} \tag{3.2.4}$$

where α is the angle between **y*** and **y'***, and β the angle between **n̂*** and **y'***. **n̂*** is then converted into cartesian coordinates in real space by multiplying it with a transformation matrix M. In an orthorhomic system M is given by
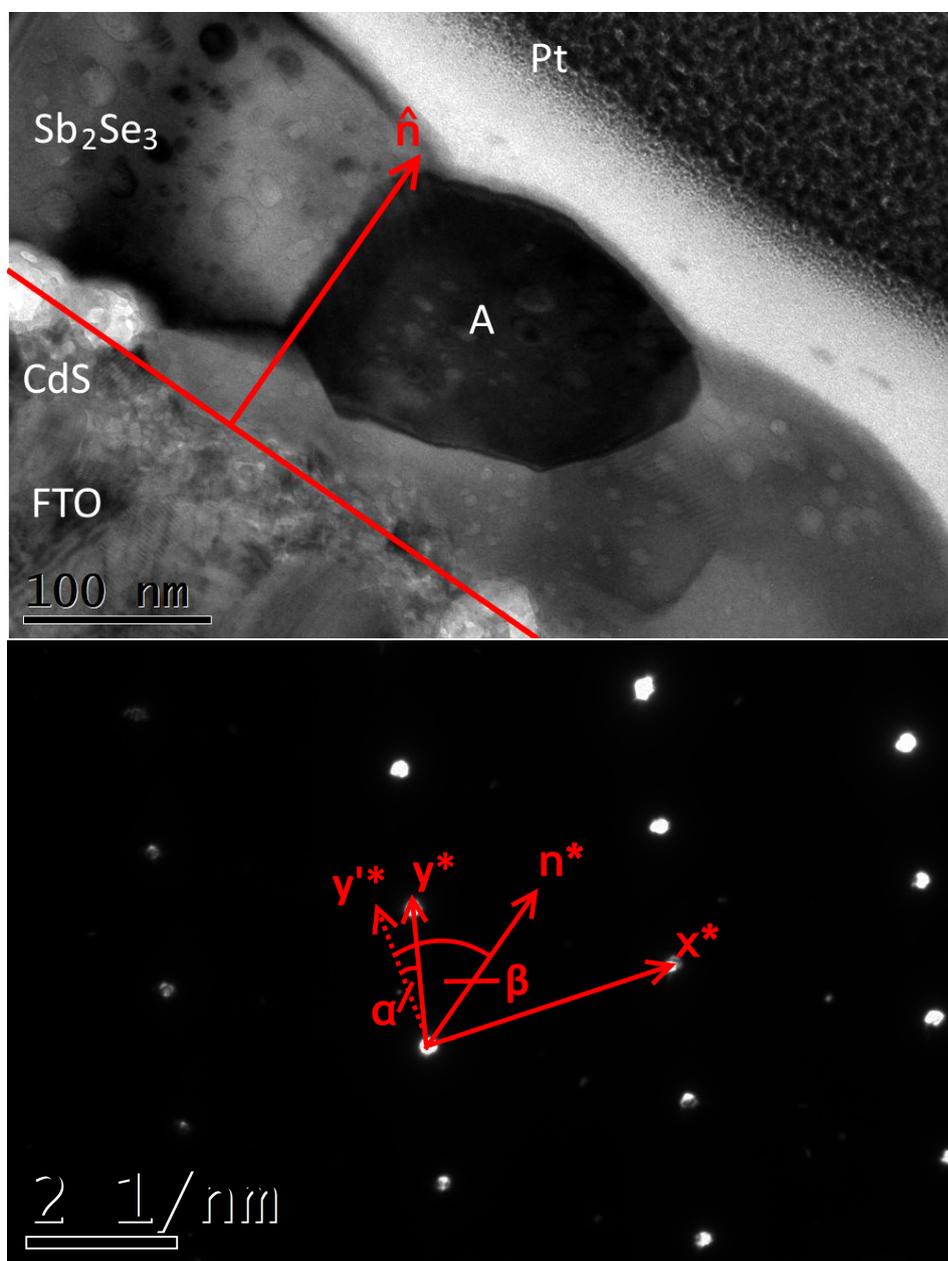
Figure 3.2: Top: Bright field image of an Sb$_2$Se$_3$ crystal (labelled 'A'), with the substrate normal marked as $\hat{\mathbf{n}}$. Bottom: Diffraction pattern obtained from this crystal, with the substrate normal $\hat{\mathbf{n}}$* superimposed. Also labelled are reciprocal lattice vectors $\mathbf{x}$*, $\mathbf{y}$*, $\mathbf{y}'$* and angles α and β.

$$M = \begin{bmatrix} |\mathbf{a}^*| & 0 & 0 \\ 0 & |\mathbf{b}^*| & 0 \\ 0 & 0 & |\mathbf{c}^*| \end{bmatrix}$$

where $|\mathbf{a}^*|$, $|\mathbf{b}^*|$, $|\mathbf{c}^*|$ are the magnitudes of the reciprocal lattice vectors of the crystal. The angle between the surface normal $\hat{\mathbf{n}}$ and the normal to the (001) plane is then calculated using the vector dot product;

$$\cos\theta = \frac{\mathbf{a} \cdot \mathbf{b}}{|a||b|} \tag{3.2.5}$$

The accuracy of this calculation can be checked for any grain oriented such that the zone axis lies in the (001) plane. In this case, the ribbons will be orthogonal to the beam direction, so using HREM imaging it is possible to directly measure their orientation relative to the surface normal, and compare with the calculated value. It was found that the HREM and electron diffraction orientation values were in good agreement, being within 4° of each other.

Estimating the error

The method outlined above for calculating the orientation of the ribbons assumes that the interface plane lies parallel to the beam direction. However, because the sample has to be tilted to make the beam line up with a low order Sb_2Se_3 zone axis, this is not the case and introduces an error in the calculated result. This error can be worked out using a TEM image of the interface between the absorber and emitter layers.

As illustrated in Figure 3.3, the tilt of the sample causes the absorber and emitter layers to overlap for a short distance in the electron transparent sample. If the width of this overlap region is measured, the error E_θ can be calculated using a simple trigonometric relationship $\tan E_\theta = \frac{t}{W}$, where W is the width of the overlap, and t the thickness of the sample (assumed to be 100 nm).

Because of the requirement that the sample be relatively thin at the interface in order to image the overlap at high resolutions, this method could not be employed for all grains. The largest errors calculated by this method were $\approx$10°, which is the order of magnitude of the largest tilts employed to obtain the diffraction pattern. Hence where the error cannot be accurately determined it is assumed to be 10°.
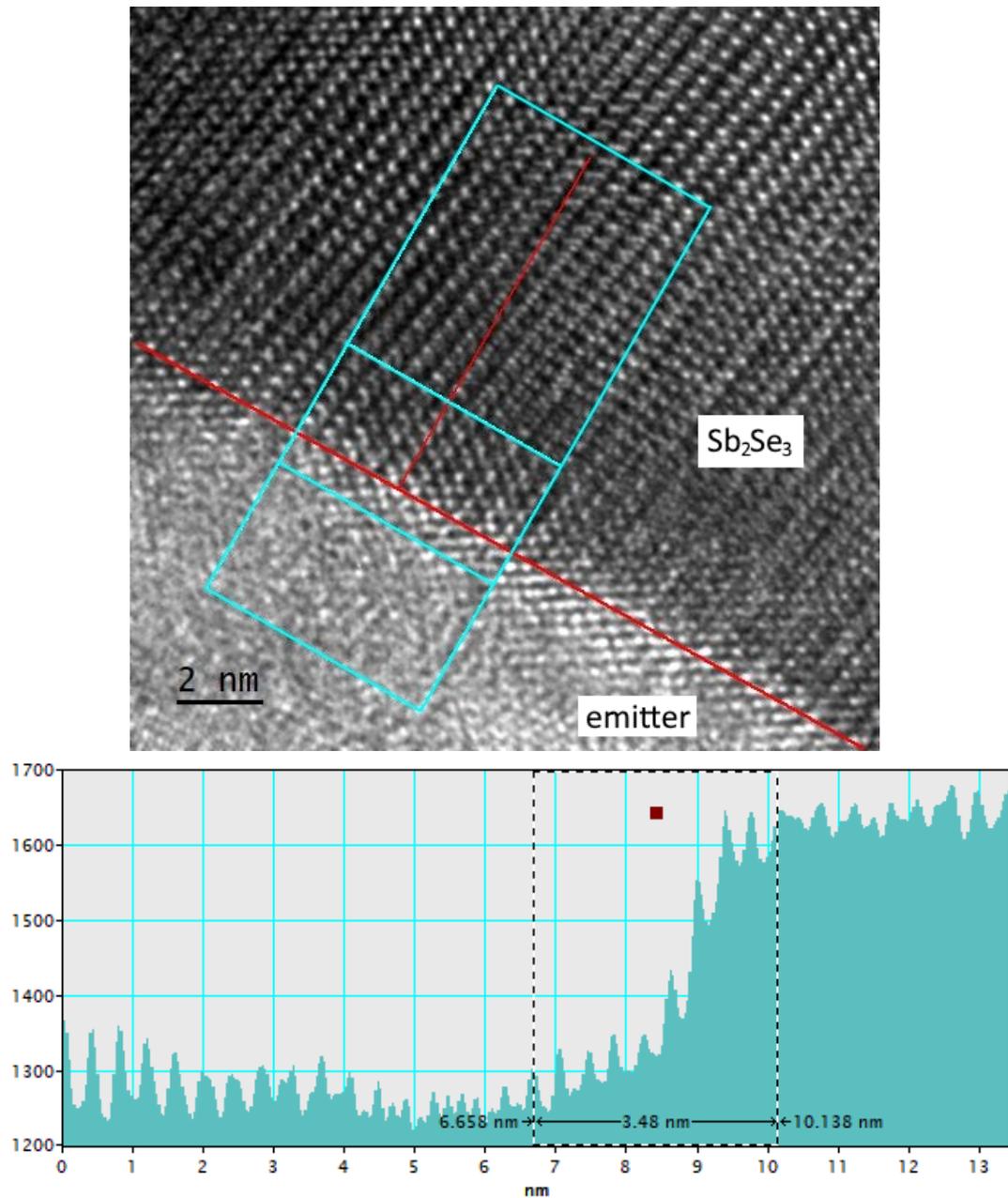
Figure 3.3: HREM image showing the Sb_2Se_3-emitter layer interface. The red lines indicate the interface and the normal. An intensity profile along the normal taken from the blue box is shown below. The width of the crossover region is indicated on both images and is around 3.48 nm.

Because the electromagnetic lens can rotate the image and diffraction pattern, it was necessary to measure the rotation between the diffraction pattern and image to ensure that the crystal orientations were accurate. This calibration involves the use of MoO_3 nanorods, and is described in section 3.2.3.

3.2.3 Image rotation calibration using MoO_3.

In an electron microscope images and diffraction patterns can be rotated relative to one another. This is due to the incident electrons moving along a helical path within the magnetic field of an electromagnetic lens. In order for the method of determining the interface normal (section 3.2.2) to be accurate the extent of this rotation must be known. This is found using molybdenum oxide crystals. As shown in Figure 3.4, these are take the form of 'needles', and the long axis of the 'needle' is always perpendicular to the shortest spacing in the diffraction pattern. As the image rotation can vary for different magnifications and camera lengths the crystals and diffraction patterns must be viewed at each available setting [59]. Figure 3.4 shows a MoO_3 'needle' imaged at 8,000×, and the corresponding diffraction pattern at a camera length of 50 cm. For this combination of settings the rotation was around 4°. This was found to be the case also for camera lengths from 50 cm to 80 cm and magnifications from 4,000× to 800,000×. This constant rotation offset of 4°was taken into account when calculating the Sb_2Se_3 ribbon orientation.

Figure 3.4: Top: image of a MoO$_3$ crystal tilted to zone axis, captured at 8,000×
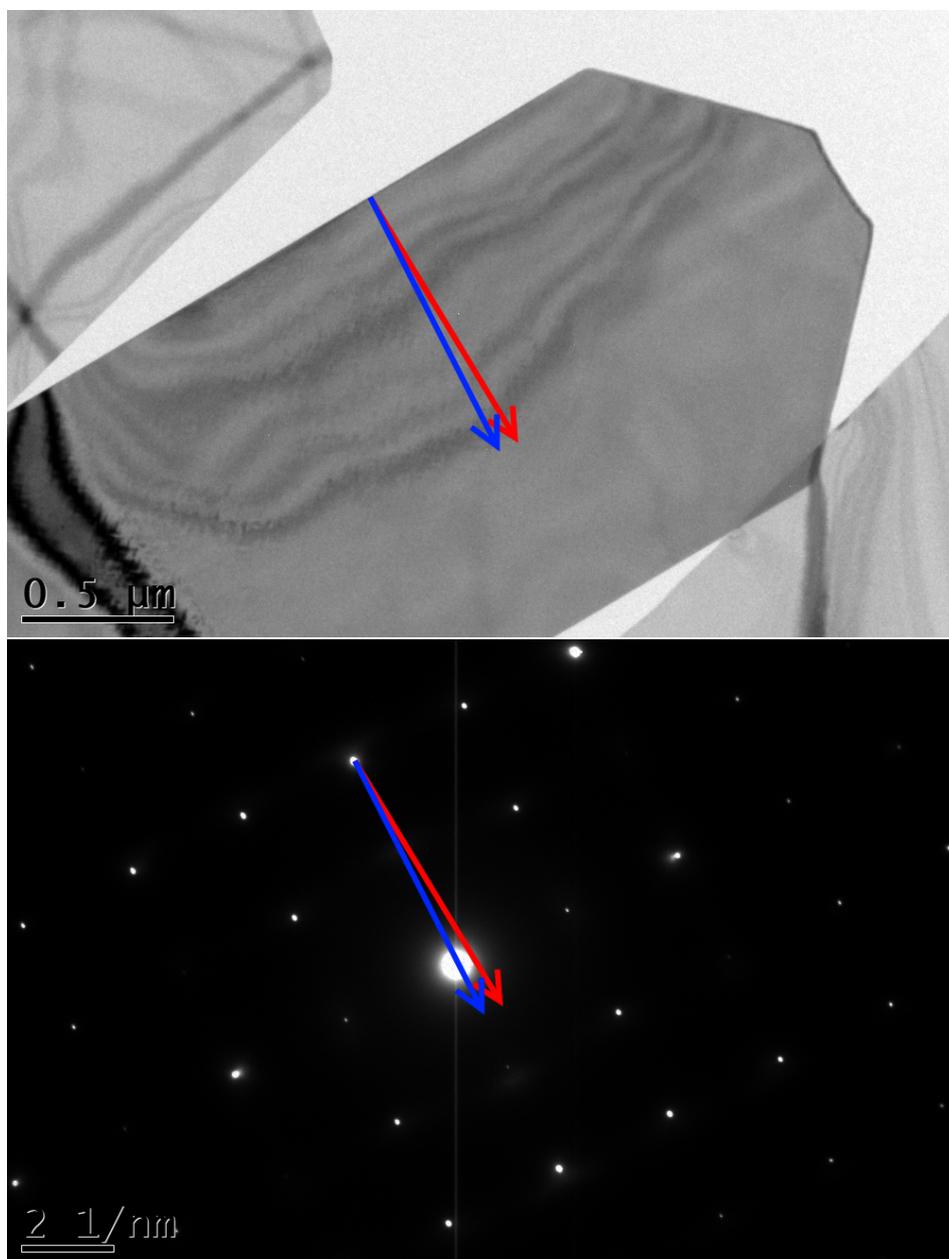magnification. Bottom: Diffraction pattern obtained from this crystal at camera length
50 cm. On both images a line perpendicular to the long axis is marked in red, and the
short vector in the diffraction pattern is marked in blue.

Chapter 4

Experimental Results and Discussion

4.1 Sample A (CdS - CSS Sb_2Se_3)

4.1.1 SEM images

Figure 4.1 shows top down and cross-sectional SEM images of sample A. The top down image, Figure 4.1(a), shows that the Sb_2Se_3 layer consists of large (≈ 1 µm in diameter) irregularly shaped grains. There are apparent pinholes between the grains; however, the cross-sectional images show that these do not extend through the entire film thickness. The cross-sectional images (b,c) show the Sb_2Se_3 layer to be up to 4 µm thick. The CdS layer is ≈ 100 nm thick and appears to be composed of roughly 'equiaxed' grains. The ZnO layer is ≈ 200 nm thick and the fluorine-doped tin oxide (FTO) ≈ 500 nm thick. Significantly, large amounts of Sb_2Se_3 have dissolved, leaving a gap ≈ 300 nm thick running across the entire length of the CdS-Sb_2Se_3 interface. This implies significant levels of interdiffusion from the Sb_2Se_3 to the CdS (shown by EDX data, Chapter 4 Section 4.1.3). The vertical lines visible in Figure 4.1(c) are a result of FIB milling.

4.1.2 TEM

Figure 4.2 (a,b) shows STEM bright-field and dark-field images of sample A. The Sb_2Se_3 grain boundaries are clearly visible, showing that although the sample is primarily composed of columnar grains with grain boundaries perpendicular to the substrate, the sample appears to have a competetive growth texture in which there are a number of smaller
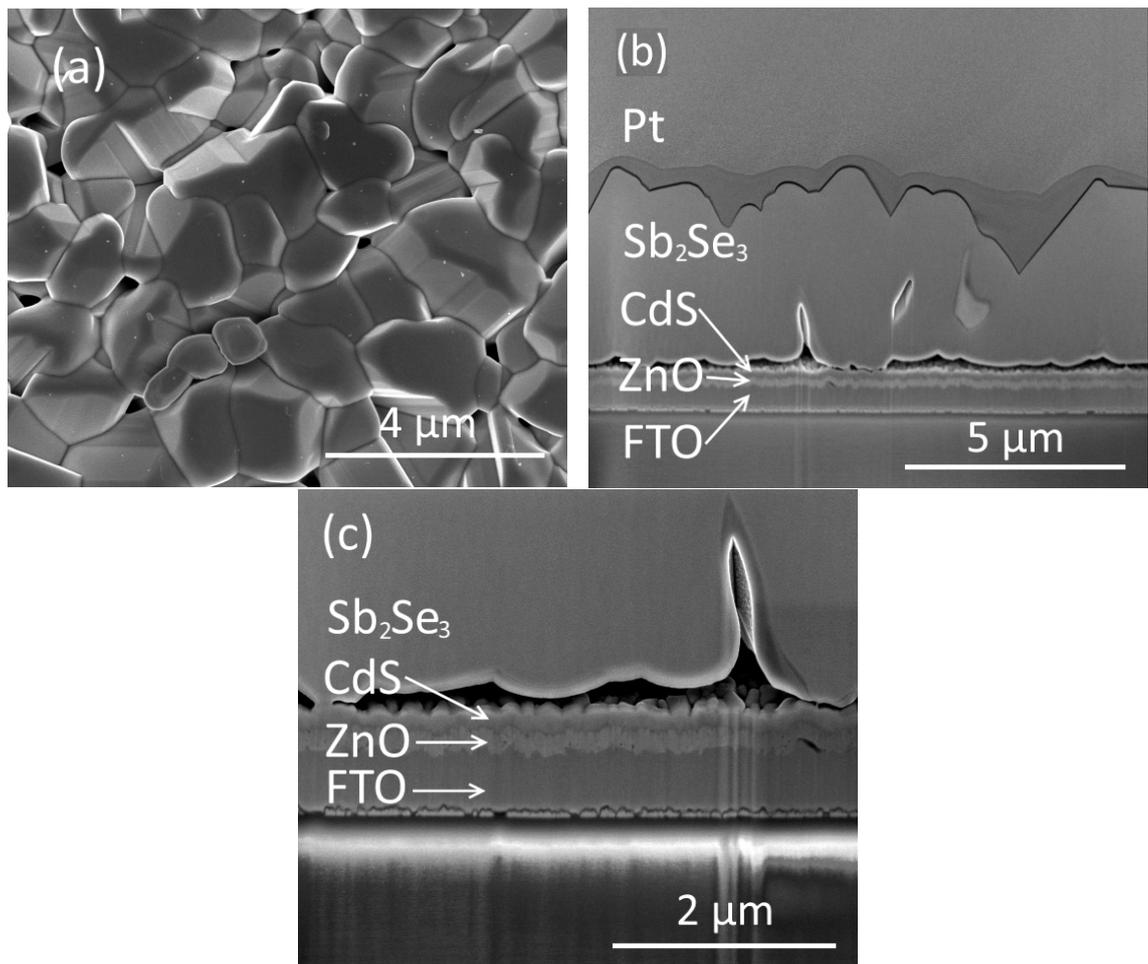
Figure 4.1: (a) top down SEM image of sample A. (b) cross-sectional SEM image of sample A. The Pt layer is from FIB sample preparation. (c) higher magnification image of voiding at CdS/Sb$_2$Se$_3$ interface.
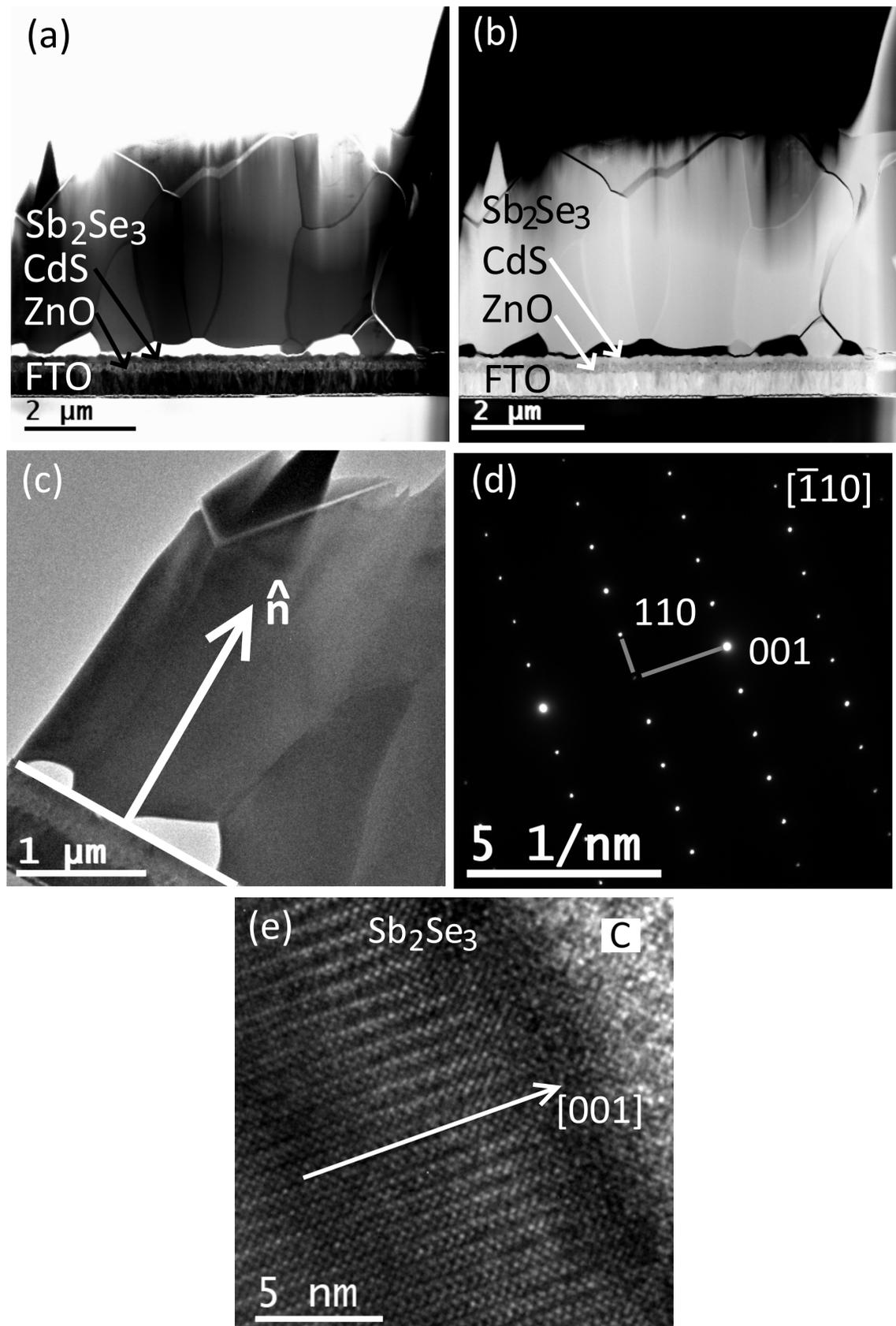
Figure 4.2: STEM bright-field (a) and dark-field (b) images of sample A. (c) conventional TEM image with the interface normal indicated by white arrow. (d,e) indexed diffraction pattern and HREM images with the [001] direction indicated for a grain in sample A. Carbon layer in (e) is due to FIB sample preparation.

grains close to the CdS interface, with some grain boundaries running approximately parallel to substrate.

Figure 4.2 (d,e) shows an indexed diffraction pattern and HREM image of a grain in sample A. Using the interface normal in Figure 4.2 (c), the orientations of this grain, and 8 others were found via the method described in section 3.2.2, Chapter 3. The [001] ribbon direction of the grain shown in Figure 4.2 has an orientation of 41±8° relative to the interface normal. For this sample, the mean ribbon orientation is 32° with a standard deviation of 8°.

4.1.3 STEM EDX

Figures 4.3 (b-h) show STEM-EDX maps of Se, Sb, Cd, S, Zn, O and Sn, and Figure 4.3 (i) an EDX linescan of these elements along the line indicated in Figure 4.3 (a). It is clear that there is significant diffusion of Se and Sb into the CdS emitter layer of the sample. The Se shows a negative concentration gradient from the top to the bottom of the emitter layer, however the Sb is concentrated at the CdS-ZnO interface. The Sb signal from the FTO layer in Figure 4.3 (c) is likely due to overlap between the Sb Lα and Sn Lα X-ray energies (3.6 keV and 3.4 keV respectively) [65].

In both the maps and the linescan there is a clear separation between the Se and S at the top of the CdS layer, indicating the substitution of Se for S. Whilst the Sb and S peaks overlap on the linescan, and the S peak is offset from the Cd peak, which may indicate the S separating from the CdS to form a layer of Sb$_2$S$_3$, they appear to be separated horizontally on the maps. Furthermore, there is no correlation between the Sb and Cd maps, which suggests that the Sb is not incorporated into the CdS crystal structure. It is unclear from the maps whether any S has separated from the Cd(S,Se) layer.

Figure 4.4 (b) shows a linescan along the length of the white line, from the bottom of the ZnO layer to the top of the small grain, shown in Figure 4.4 (a). Since the widths of the Cd and S line profiles are similar, it follows that there is no diffusion from the CdS layer to the Sb$_2$Se$_3$ layer, and the Se and Sb lines show the ratio of Se to Sb to be constant throughout the thickness of the Sb$_2$Se$_3$ grain. As the X-ray signal is normalised, no conclusions about the ratios of elements in the sample can be drawn. Within the emitter layer the linescan shows similar trends to those in Figure 4.3.
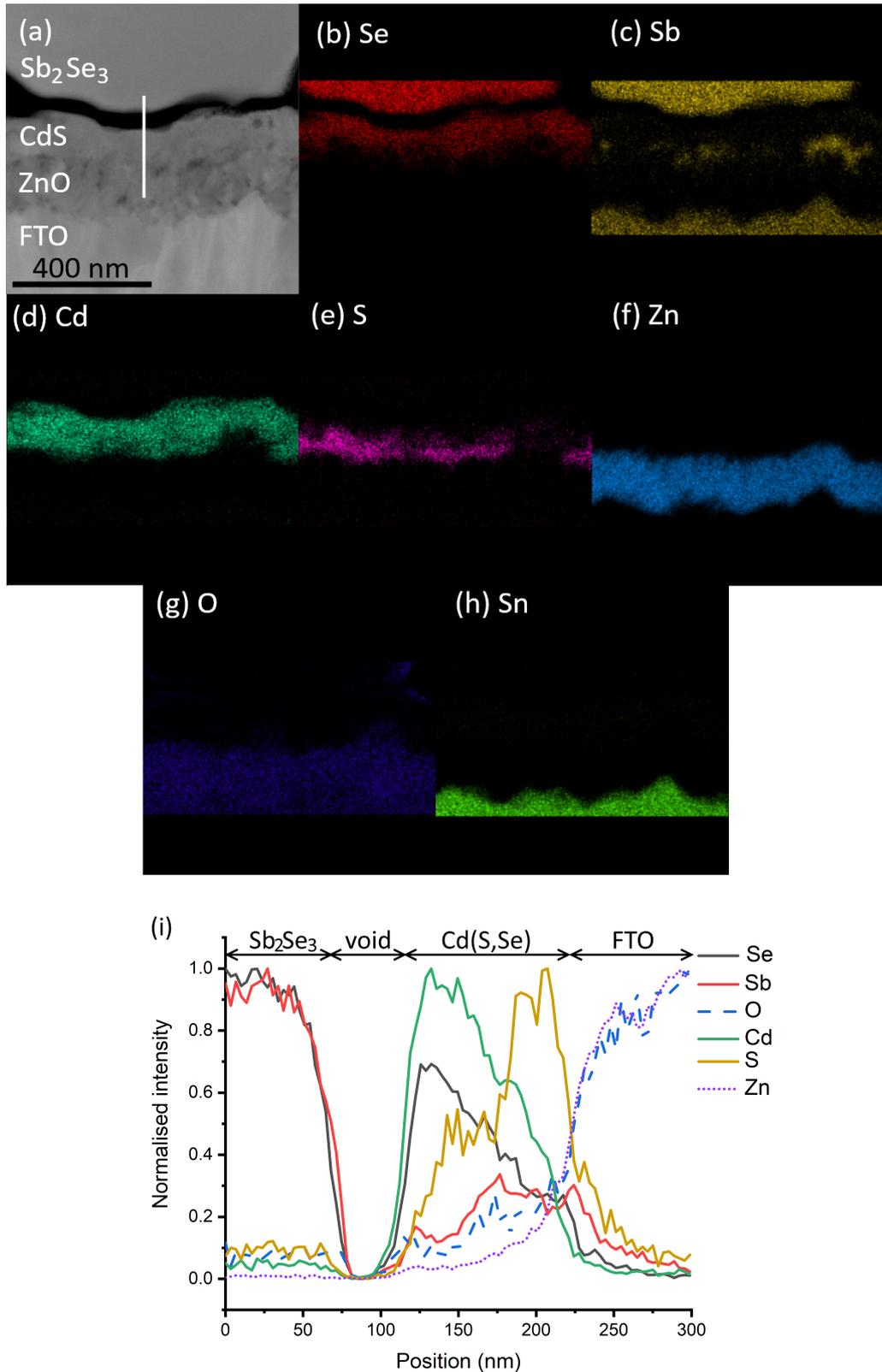
Figure 4.3: (a) STEM dark-field image of the CdS-Sb$_2$Se$_3$ interface region in sample A. (b-h) Se, Sb, Cd, S, Zn, O, and Sn EDX maps of the area shown in (a). (i) EDX linescan along the white line shown in (a). The approximate regions of the different layers are indicated in (i). Cd(S,Se) denotes the Se inter-diffused CdS emitter layer.
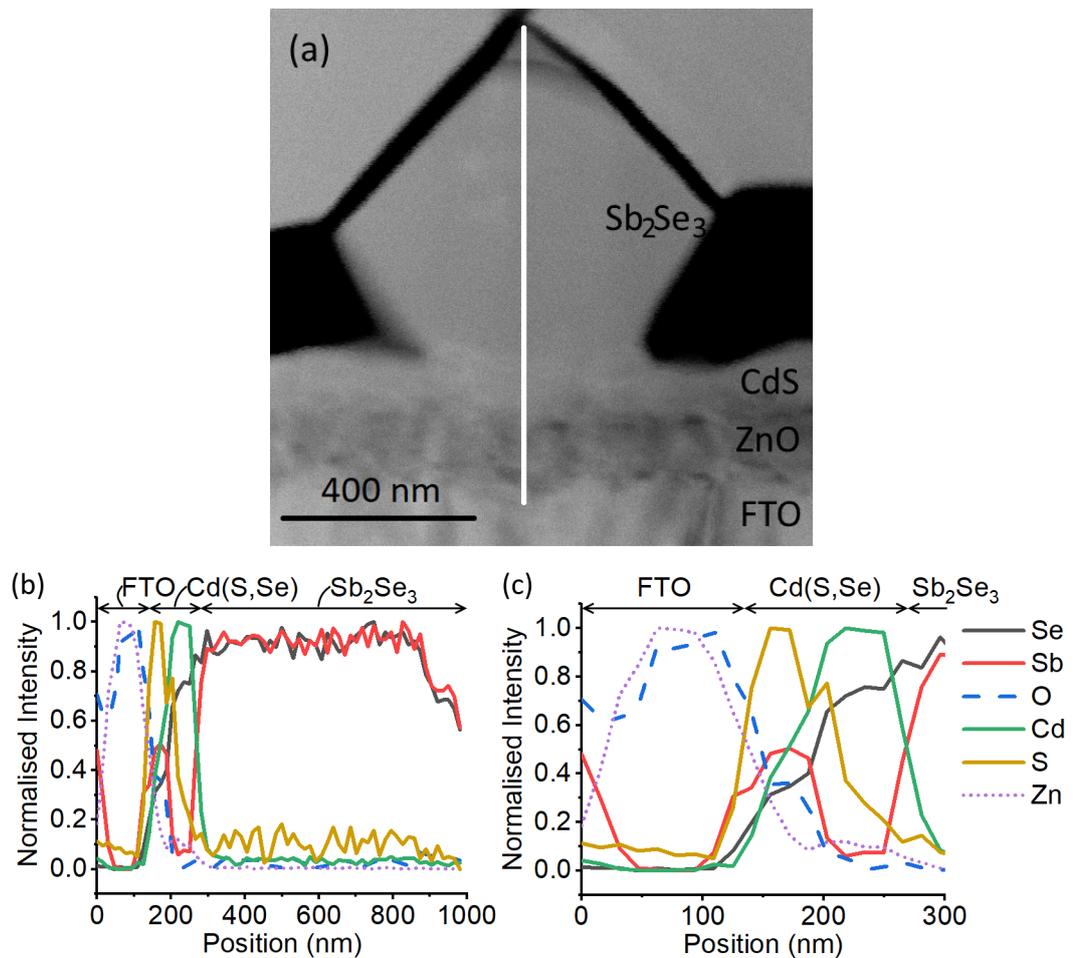
Figure 4.4: (a) STEM-DF image of an Sb$_2$Se$_3$ crystal grain, (b) EDX linescan along the white line in (a), and (c) expanded line profile of the Cd(S,Se) layer in (b). The approximate regions of the different layers are indicated in (b,c). Cd(S,Se) denotes the Se inter-diffused CdS emitter layer

Figure 4.5: (a) top down SEM image of sample B. (b) cross-sectional SEM image of sample B. The C and Pt layers are from FIB sample preparation.

4.2 Sample B (CdS - TE Sb$_2$Se$_3$)

4.2.1 SEM images

Figure 4.5 shows top down and cross-sectional SEM images of sample B. The top down image Figure 4.5 (a) shows that the Sb$_2$Se$_3$ layer consists of small grains $\approx$ 100 nm in diameter. The cross-sectional image Figure 4.5 (b) shows the Sb$_2$Se$_3$ layer to be $\approx$ 250 nm thick. The CdS layer is $\approx$ 50 nm thick and the FTO $\approx$ 500 nm thick. In contrast to the CSS sample (A) there is no voiding at the CdS-Sb$_2$Se$_3$ interface visible in Figure 4.5, and the CdS layer is much thinner, which does not suggest significant levels of interdiffusion. The small grain size and lack of interdiffusion are attributed to the lower deposition temperature of thermal evaporation compared to close space sublimation (Section 3.1).

4.2.2 TEM

Figure 4.6(a,b) shows STEM bright-field and dark-field images of sample B. The Sb$_2$Se$_3$ grain boundaries are clearly visible, showing the sample to be primarily composed of columnar grains. The grain interiors are not fully dense and contain numerous small voids. There are a small number of voids visible at the CdS-Sb$_2$Se$_3$ interface, although much less than are visible in sample A. In contrast to sample A, where the CdS layer is dense, in this sample the CdS layer shows a large number of internal voids, as evidenced by the dark 'dots' in Figure 4.6 (b).

Figures 4.6(c,d,e) show a TEM bright-field image, indexed diffraction pattern, and
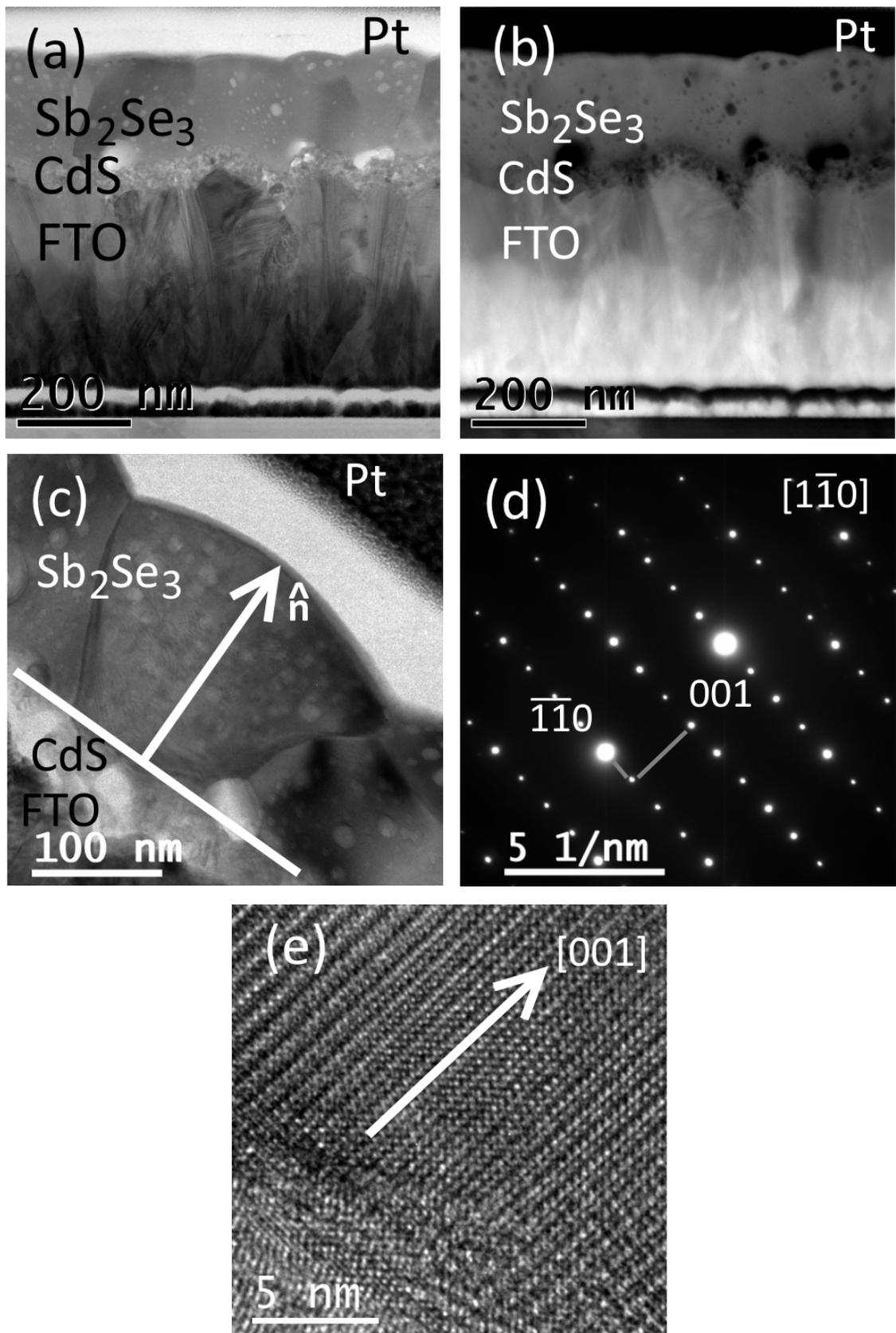
Figure 4.6: (a,b) STEM bright-field and dark-field images of sample B. (c) TEM bright-field image of a grain in sample B, with the interface normal indicated; (d,e) indexed diffraction pattern and HREM image of the grain shown in (c), with the [001] direction indicated.
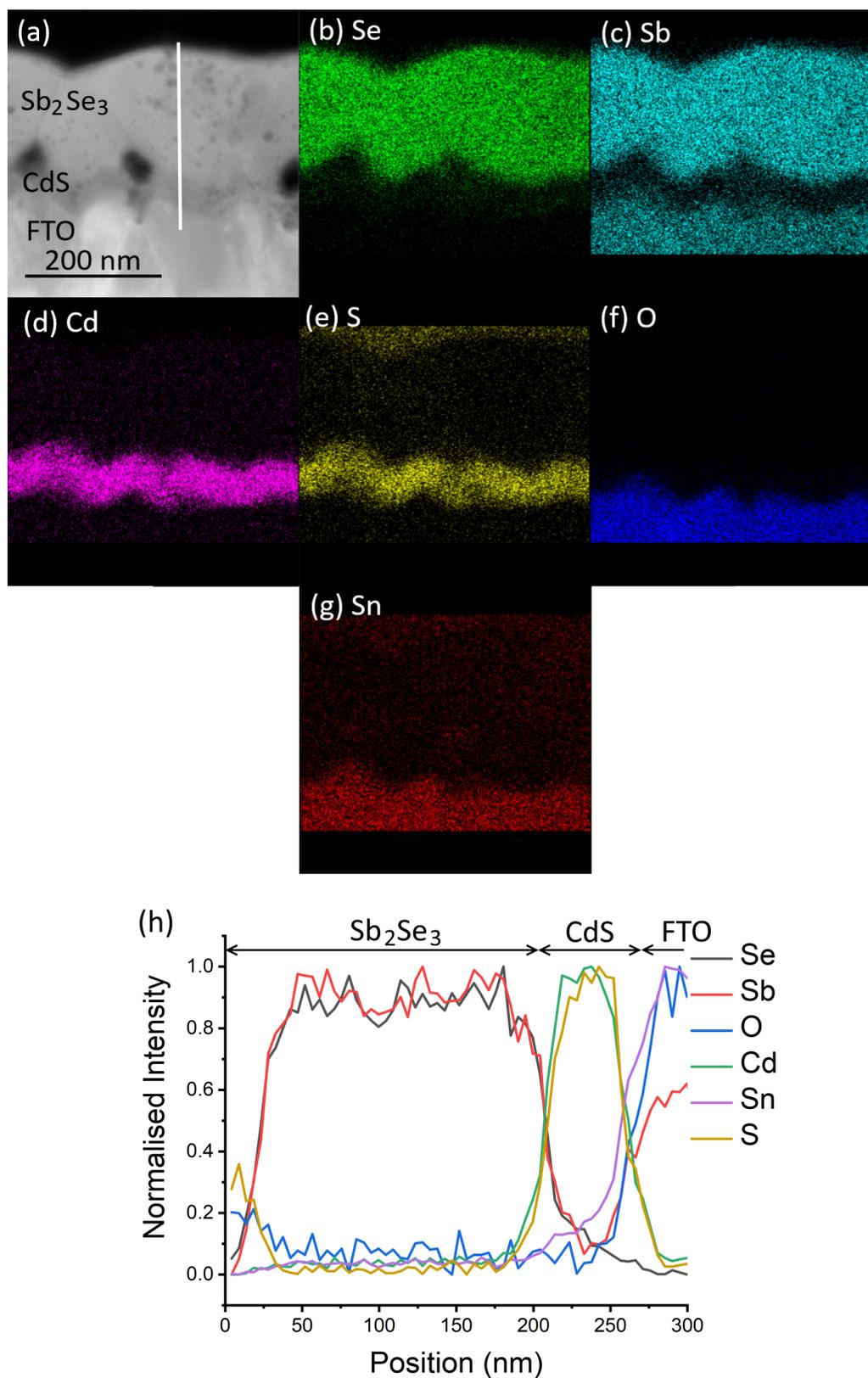
Figure 4.7: (a) STEM dark-field image of the Sb$_2$Se$_3$ and CdS layers in sample B. (b-g) Se, Sb, Cd, S, O, and Sn EDX maps of the area shown in (a). (h) EDX linescan along the white line shown in (a).
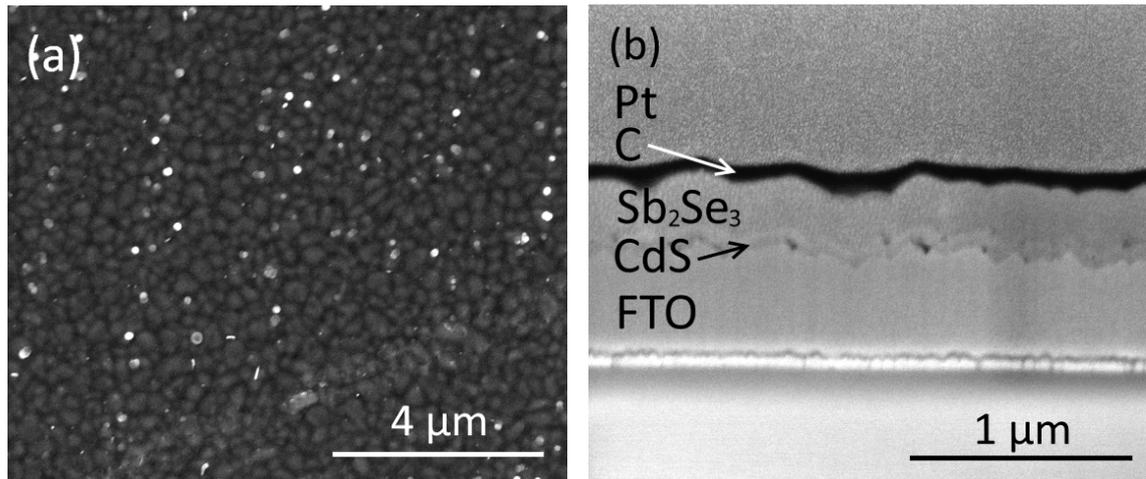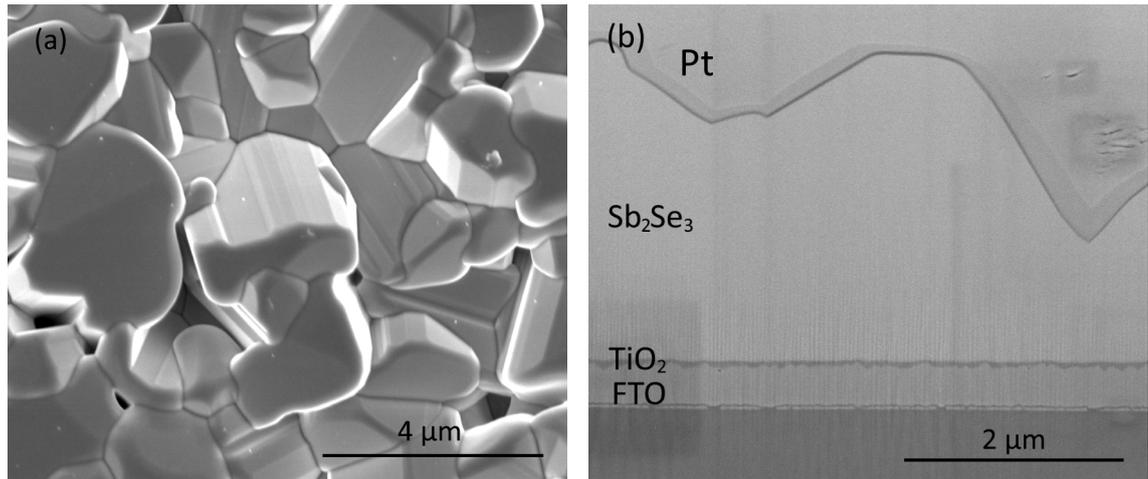
Figure 4.8: (a) top down SEM image of sample C. (b) cross-sectional SEM image of sample C. The Pt layer is from FIB sample preparation

HREM image of a grain in sample B. The ribbon orientation of this grain relative to the CdS-Sb$_2$Se$_3$ normal is 8$\pm$6°. For this sample, the mean ribbon orientation is however 44° with a standard deviation of 19°.

4.2.3 STEM EDX

Figure 4.7 shows EDX maps and linescans of Se, Sb, Cd, S, Sn, and O for sample B. Although the maps appear to show diffusion of Se and Sb into the CdS layer, the linescan shows no separation of Se and Sb or of Cd and S. Furthermore, the intensity of the Se signal from the CdS layer is much lower in sample B than sample A, indicating lower levels of diffusion in the TE sample. As in sample A, the strong Sb signal from the FTO layer is due to the similar energies of the Sb and Sn X-rays.

4.3 Sample C (TiO$_2$ - CSS Sb$_2$Se$_3$)

4.3.1 SEM images

Figure 4.8 shows top down and cross-sectional SEM images of sample C. The top down image, Figure 4.8(a), shows that the Sb$_2$Se$_3$ layer consists of large (>1 µm in diameter) irregular grains, similar to sample A. The cross-sectional image, Figure 4.8(b), shows the Sb$_2$Se$_3$ layer to be $\approx$ 2-3 µm thick. In contrast to the other CSS sample (A), there is no visible porosity at the Sb$_2$Se$_3$-emitter interface. The TiO$_2$ layer is $\approx$ 50 nm thick and the FTO $\approx$ 500 nm thick.

4.3.2 TEM

The STEM images (Figure 4.9 (a,b)) show the sample to be mainly composed of large columnar grains, similar to sample A. There is however a signigicant difference in size between some of the grains. For example there is a smaller grain (grain 2) trapped beneath a larger grain (grain 1), as indicated in Figure 4.9. This grain (grain 2) has a rounded shape, unlike the larger columnar grains seen in sample A.

Figure 4.9 (c,d,e) shows the TEM bright-field image and indexed diffraction patterns of the two grains labelled in Figure 4.9 (b). The ribbon orientation of the large grain relative to the substrate is 20±10°, while that of the small grain is 70±10°. The mean ribbon orientation for this sample is 42° with a standard deviation of 18°.

4.3.3 STEM EDX

Figure 4.10 shows EDX maps and linescans of Se, Sb, Ti, O, and Sn for sample C. These show the TiO$_2$-Sb$_2$Se$_3$ interface to be abrupt, with no signs of interdiffusion. For example, there is no separation of the Sb, Se and Ti, O linescan profiles. Again the strong Sb signal from the FTO layer is due to the similar energies of the Sb and Sn X-rays.

4.4 Sample D (TiO$_2$ - Sb$_2$Se$_3$ seed layer)

4.4.1 SEM images

Figure 4.11 shows top down and cross-sectional SEM images of sample D. The top down image (a) shows that the Sb$_2$Se$_3$ layer consists of very small grains, approximately 100 nm in size. The grains have numerous gaps between them. This is confirmed by the cross-sectional image (b), which shows the Sb$_2$Se$_3$ seed layer to be $\approx$ 100 nm thick. The TiO$_2$ layer is $\approx$ 50 nm thick and the FTO $\approx$ 500 nm thick.

4.4.2 TEM

Figure 4.12 (a,b) show STEM bright-field and dark-field images of sample D. A TEM bright-field image, with the TiO$_2$-Sb$_2$Se$_3$ interface normal indicated, of the grain circled in (b) is shown in (c) along with an indexed diffraction pattern in (d). The ribbon orientation of this grain relative to the interface normal is 80±3°. The mean ribbon orientation of this sample was found to be 58° with a standard deviation of 24°. The larger standard deviation is due to the orientation being determined for only 3 grains. As the grain
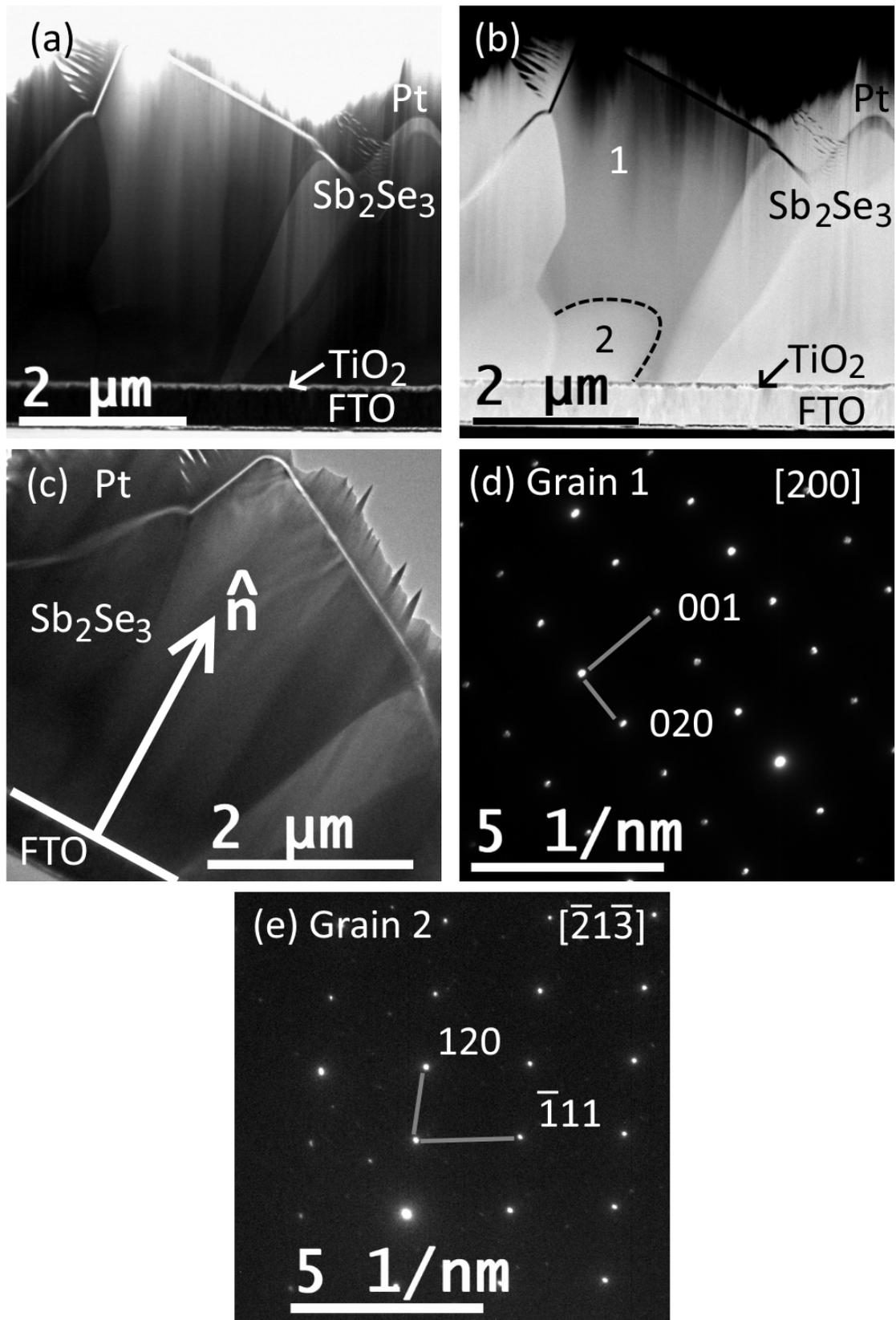
Figure 4.9: (a,b) STEM bright-field and dark-field images of sample C, with a large and small grain labelled 1 and 2. (c) TEM bright-field image of sample C with the TiO$_2$-Sb$_2$Se$_3$ interface normal marked by a white arrow. (d,e) indexed diffraction patterns of grains 1 and 2 respectively.
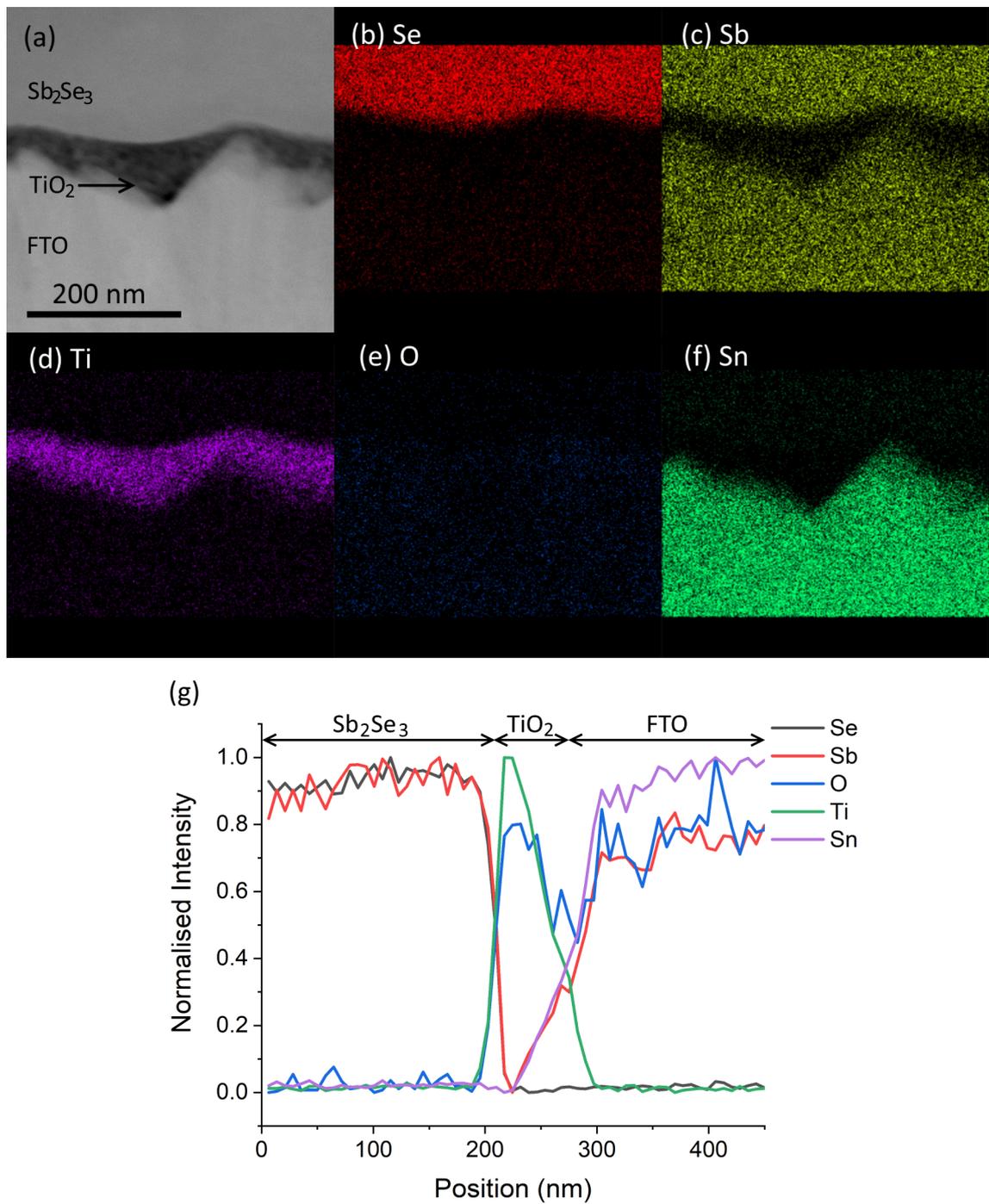
Figure 4.10: (a) STEM dark-field image of the TiO$_2$-Sb$_2$Se$_3$ interface region in sample C. (b-f) Se, Sb, Ti, O, and Sn EDX maps of the area shown in (a). (g) EDX linescan along a 500 nm line around the TiO$_2$ layer acquired from a different region of the sample.
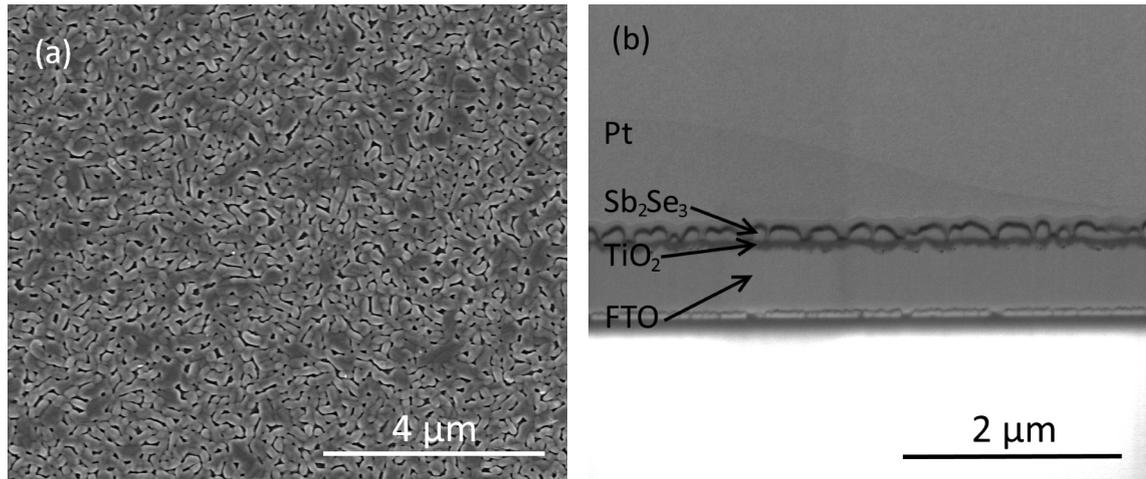
Figure 4.11: (a) top down SEM image of sample D. (b) cross-sectional SEM image of sample D. The Pt layer is from FIB sample preparation.

diameter and TEM sample thickness were similar (both around 100 nm), this meant the cross-section would often contain more than one grain stacked parallel to the specimen thickness, making it often difficult to obtain diffraction patterns.

4.4.3 STEM EDX

Figure 4.13 shows EDX element maps and linescans for sample D. The Sb_2Se_3 interface is abrupt, with no visible interdiffusion. The Sb signal from the FTO layer is due to the similar energies of the Sb and Sn X-rays.

4.5 Discussion

4.5.1 Porosity and Interdiffusion

The significant dissolution of the Sb_2Se_3 layer in sample A is believed to be due to interdiffusion and to be an example of Kirkendall voiding [67]. As the antimony and selenium atoms diffuse from the absorber to the emitter layer of the sample, vacancies diffuse in the opposite direction. These vacancies can cluster together leading to the formation of voids. This often requires the presence of impurities for the nucleation of voids; however, lattice mismatch at the $CdS-Sb_2Se_3$ interface could similarly provide nucleation sites, leading to the large voids seen across almost the entire width of the cross-section in sample A [67]. The smaller voids at the $CdS-Sb_2Se_3$ interface, and the internal porosity of the Sb_2Se_3 grains are probably due to the low susbtrate temperature
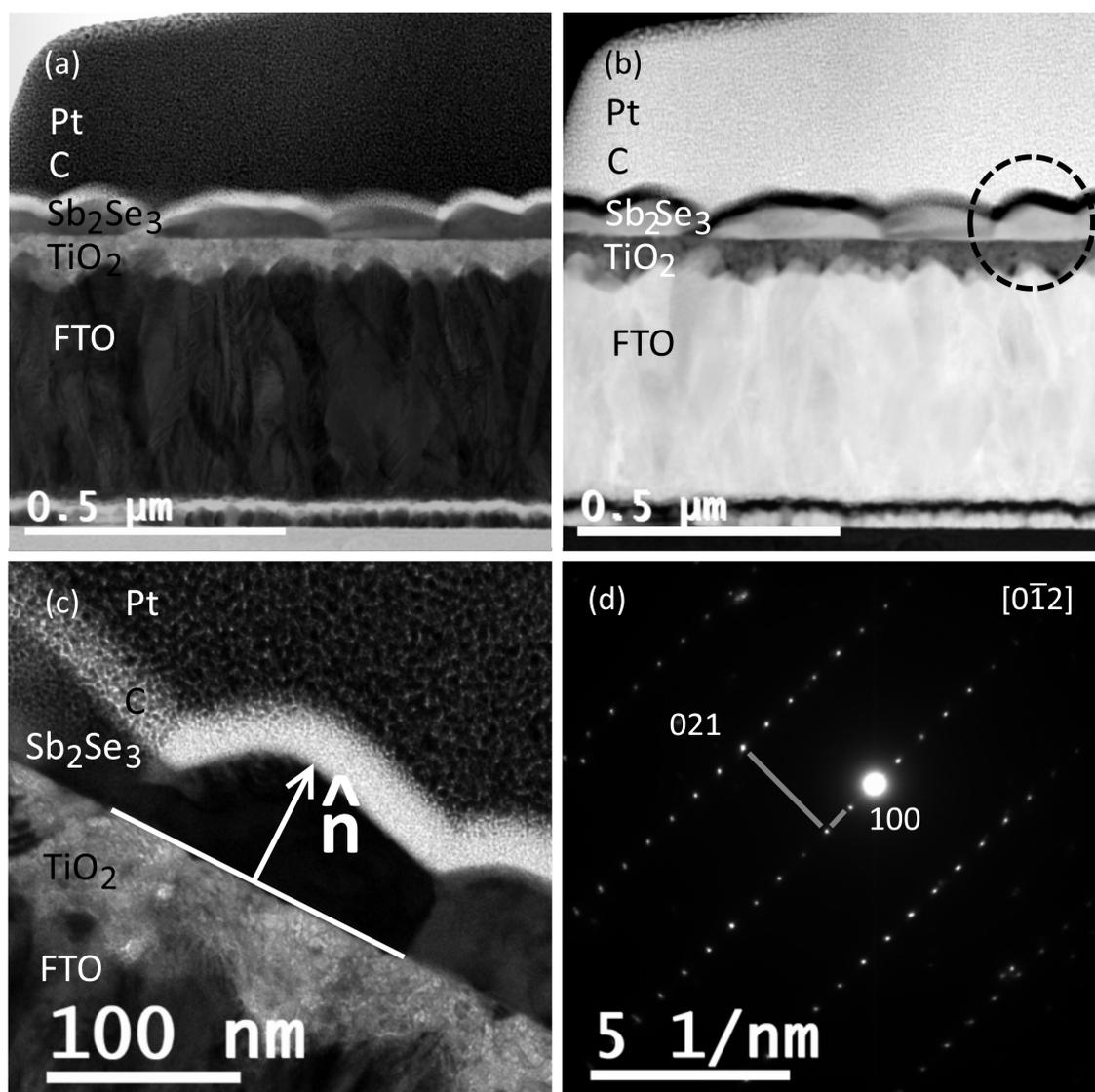
Figure 4.12: (a,b) STEM bright-field and dark-field images of sample D. (c) TEM bright-field image of the grain circled in (b), with the TiO_2-Sb_2Se_3 interface normal indicated by an arrow. (d) indexed selected area diffraction pattern of the grain shown in (c).
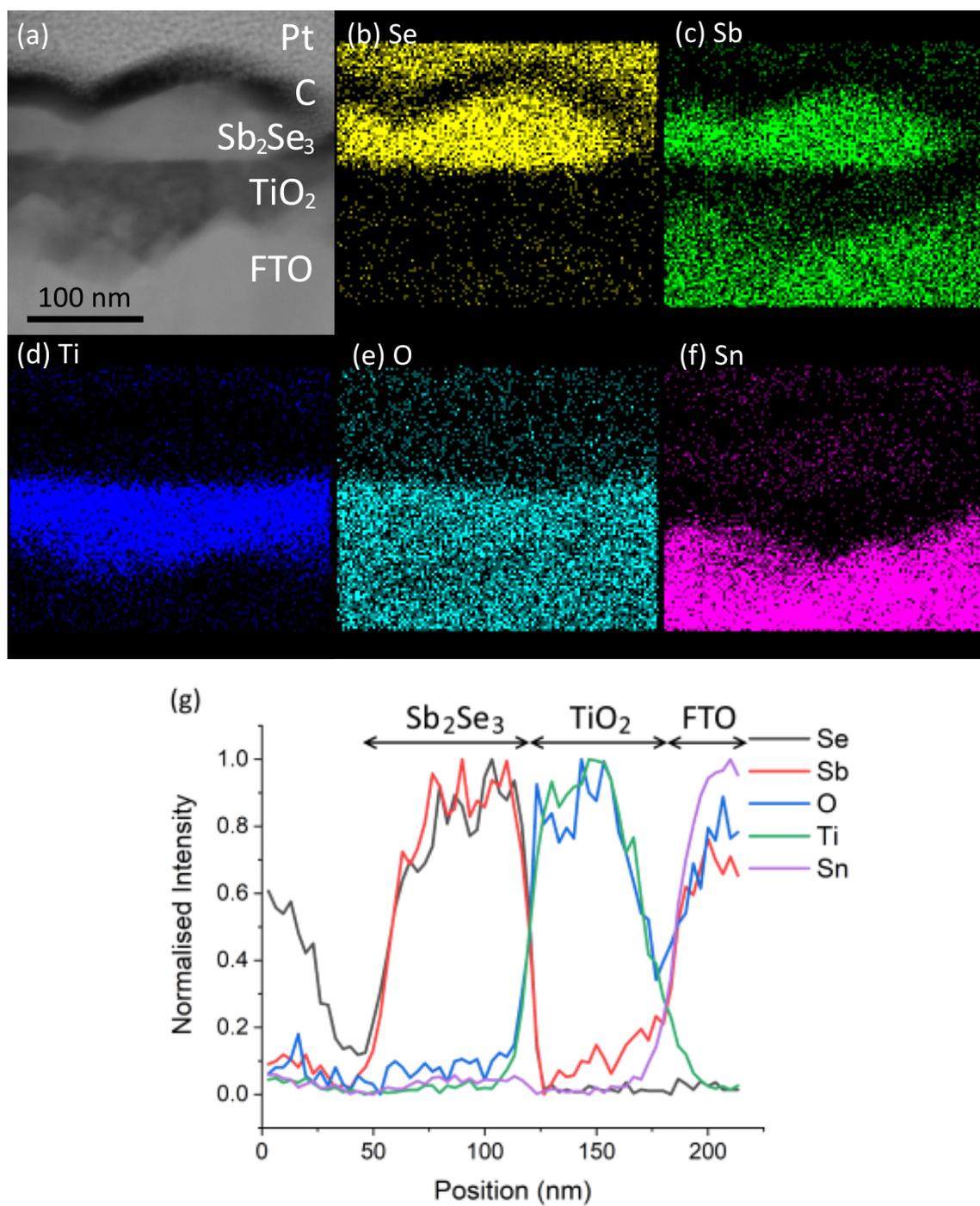
Figure 4.13: (a) STEM dark-field image of sample D; the C and Pt layers are from FIB sample preparation. (b-f) Se, Sb, Ti, O, and Sn EDX maps of the area shown in (a). (g) EDX linescan along a 200 nm line around the TiO$_2$ layer acquired from a different region of the sample.

Figure 4.14: Normalised EQE curves for samples A-C [38,45]. Results obtained by Laurie Phillips, Peter Yates, and Oliver Hutter, University of Liverpool.

in TE deposition.

In sample A, the antimony is observed to diffuse across the CdS layer and concentrate at the ZnO-CdS interface. This could be due to the large size of antimony atoms causing strain in the CdS crystal lattice, which can be relieved by segregation at the edge of the CdS layer. This is not observed in sample B, although the large false antimony signal from the FTO layer would make this difficult to detect. Although the line profile (Figure 4.3(i)) suggests the formation of a possible antimony sulfide layer, the element maps (Figure 4.3(c-e)) show clear separation between Sb and Cd, S, proving that this is not the case.

The selenium can however be substituted for sulphur to form CdSe, which has the same crystal structure (Wurtzite) as CdS, with very similar lattice parameters (CdSe, $a = 0.43$ nm, $c = 0.70$ nm; CdS, $a = 0.41$ nm, $c = 0.67$ nm) [68,69]. This allows for the formation of a Cd(S,Se) interdiffused layer as observed in the EDX data for sample A (Figure 4.3). The presence of Cd(S,Se) alters the electronic band structure of the cell to produce a potential barrier, which impedes the flow of charge carriers across the junction [38].

Because of the 1.75 eV band gap of CdSe [70], the lower bandgap of Cd(S,Se) compared to CdS also causes a drop in EQE at wavelengths below ≈ 600 nm or 2.07 eV, compared to the TiO_2 sample (as seen in Figure 4.14). This combination of a potential barrier, reduced EQE, and the significant porosity at the CdS-Sb_2Se_3 interface is likely the cause of the poor performance of sample A.

Sample	Number of grains analysed	Mean Orientation (°)	Standard Deviation (°)
A	9	32	8
B	8	44	19
C	7	42	18
D	3	58	24

Table 4.1: Mean orientation and standard deviation of the [001] direction relative to the substrate normal for each sample investigated

As no interdiffusion is observed in the TE sample (sample A), the reduced EQE of this sample at wavelengths below ≈ 700 nm cannot be explained in the same way. Instead the shape of the EQE curve may be due to poorer crystal quality, however more data such as carrier lifetime would be required to confirm this.

No interfacial porosity or interdiffusion is observed in the samples grown on TiO_2, and sample C has good peak efficiencies (6.19%) compared with sample A (1.44%), demonstrating that use of a TiO_2 layer effectively eliminates diffusion and significantly improves performance.

4.5.2 Grain Size and Orientation

The two complete CSS samples, A and C, were found to have Sb_2Se_3 layers 2-4 μm thick. Previous work has found the optimum thickness for Sb_2Se_3 solar cells to be only 500 nm thick due to the short minority carrier diffusion length in the [221] direction [27, 29, 71]. Sb_2Se_3 is highly anisotropic, and the diffusion length is increased to ≈ 1 μm in the [001] direction [27, 41, 71], yet this is still much smaller than the absorber layer thickness. This does not seem to have significantly affected cell performance, shown by the good efficiency of sample C, possibly because a thicker absorber layer would mitigate any back surface recombination losses and increase optical absorption.

The anisotropic nature of Sb_2Se_3 also leads to a variety of surface energies for the different crystal planes in the material, indicating that there may be a preferred orientation which minimises surface energy [27]. Both complete CSS samples consist of large grains, albeit with a variety of sizes and elements of competetive growth. For sample C, the grains are significantly (over 10×) larger than the grains in the seed layer (sample D), indicating significant restructuring and grain boundary migration during the second phase of growth.
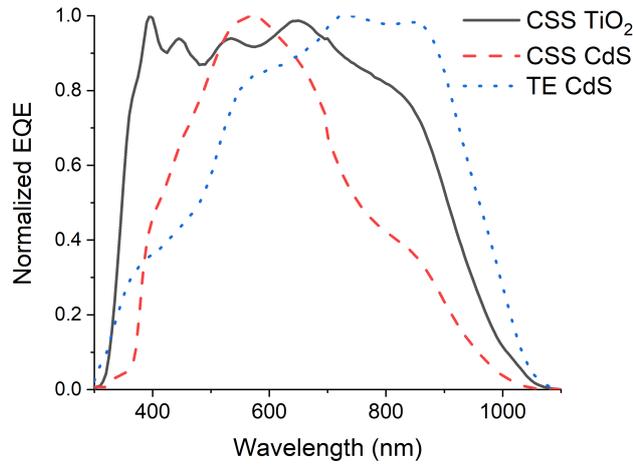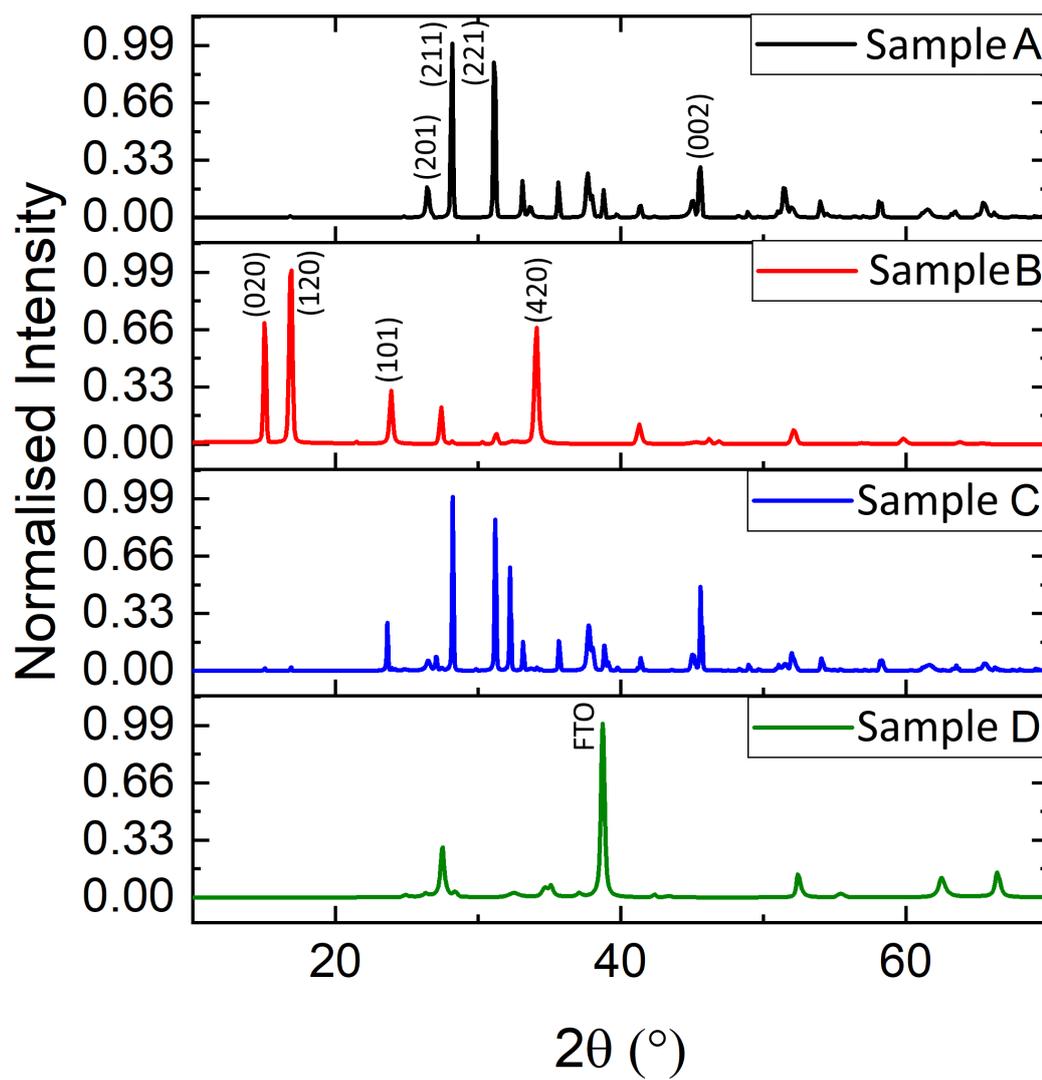
Figure 4.15: XRD patterns for samples A-D [38, 45]. Results obtained by Laurie Phillips, Peter Yates, and Oliver Hutter, University of Liverpool.
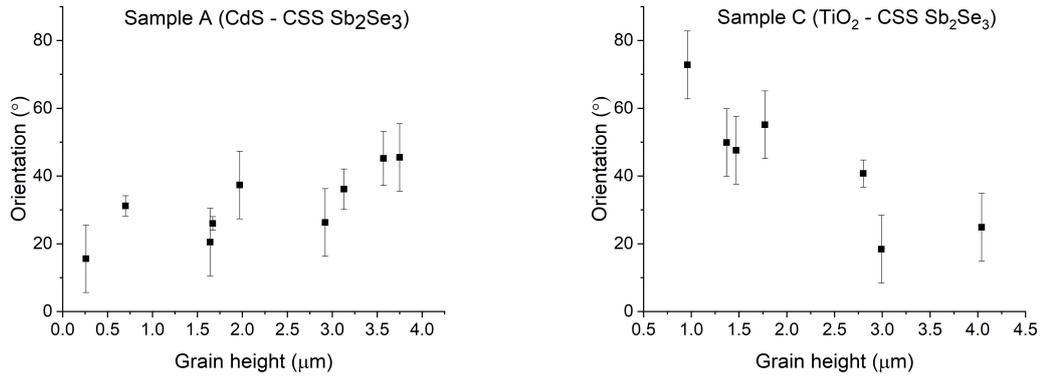
Figure 4.16: Orientation of the [001] direction relative to the substrate normal plotted against grain height for samples A and C. The same vertical axis is used in both figures.

This suggests that these CSS cells may be better oriented than the smaller grained TE cell, and that within the CSS cells the larger grains may be preferentially oriented compared with the smaller grains.

The average ribbon orientations of the four samples are summarised in Table 4.1. All samples have mean orientations within one standard deviation of one another, indicating no significant difference. X-ray diffraction (XRD) analysis was carried out at the University of Liverpool; the results are shown in Figure 4.15. The XRD patterns show strong (221) and (211) peaks for samples A, C, and D, corresponding to orientations of 37° and 44°, respectively, which is in good agreement with the values obtained from electron diffraction. The XRD pattern for sample B shows a number of strong (hk0) peaks, indicating many grains to have ribbons lying parallel to the substrate, which was not observed in electron diffraction. This could be due to the smaller sampling size for electron diffraction compared to XRD.

Figure 4.16 shows grain orientation plotted against height (i.e. grain dimension along film thickness direction) for the two close space sublimation samples (A and C). For A there is no strong correlation; however C shows a strong relationship between size and orientation, indicating that larger grains are better oriented (i.e. have ribbons more normal to the susbtrate) than smaller grains. This is likely due to the grain restructuring from the seed layer discussed previously. Examination of the XRD patterns in Figure 4.15 also shows a stronger (002) peak (corresponding to ribbons normal to the susbtrate) for sample C, consistent with the electron diffraction data. Data is not plotted for the TE sample (B) and the seed layer (D) as they lack the competitive growth texture and variety of
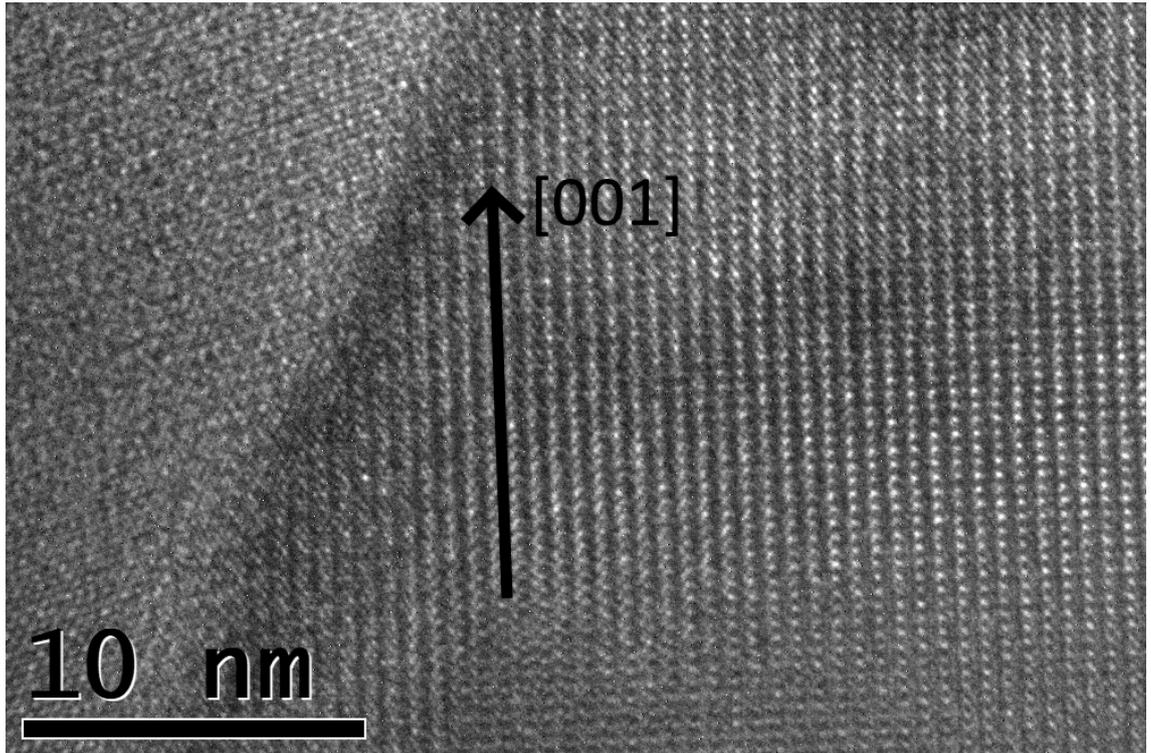
Figure 4.17: HREM image of a grain boundary in sample A, with the [001] direction (ribbon direction) indicated.

grain size of the CSS samples (i.e. nearly all grains in sample B extend throughout the entire film thickness and are $\approx$200 nm in size), and only three data points are available for sample D.

As the ribbons are tilted rather than perfectly normal to the substrate, the ribbons terminate at the grain boundaries, rather than at Van der Waals gaps. This is illustrated in Figure 4.17, which shows a grain boundary in sample A with the ribbons along [001] indicated. This could lead to dangling covalent bonds acting as recombination centres, similar to CdTe and other polycrystalline materials. Thus, although the crystal structure of Sb_2Se_3 in principle enables benign grain boundaries, the (211) and (221) texture in most thin-films precludes the elimination of grain boundary effects. Use of a seed layer can, however, help improve grain orientation towards the ideal (001) texture, although small, poorly-oriented grains remain (Figures 4.15,4.16).

Chapter 5

Summary and further work

5.1 Summary

In this project, four antimony selenide thin-films were investigated; one grown on CdS by thermal evaporation (TE), one grown on CdS by close-space sublimation (CSS), one grown on TiO$_2$ by CSS, and a seed layer grown on TiO$_2$. Of the three complete devices, the TiO$_2$-CSS device had the best efficiency, with a peak performance of 6.18%, and the CdS-CSS had the worst efficiency, 1.44%. The CdS-TE device had an efficiency of 2.85%.

An electron microscopy study was carried out to characterise these devices and understand the effect of different growth techniques and emitter layers on structure, chemical interdiffusion, grain orientation and ultimately performace. The samples were imaged using scanning electron microscopy and focused ion beam microscopy was used to prepare thin specimens for transmission electron microscopy. Scanning transmission electron microscopy was used to image grain morphology, and was combined with energy dispersive X-ray spectroscopy to measure chemical interdiffusion. Selected area electron diffraction and high resolution electron microscopy were used to find the orientation of the ribbons relative to the normal to the interface between the Sb$_2$Se$_3$ and the emitter layer (i.e. the film thickness direction).

It was found that CSS yielded a relatively thick (2-4 µm) Sb$_2$Se$_3$ layer, comprised primarily of a single layer of large ($\approx$1 µm in diameter) columnar grains, however with some indications of competetive growth. The TE device consisted of a thin ($\approx$250 nm) layer of Sb$_2$Se$_3$, composed of a single layer of small grains. Significantly, cross-sectional imaging showed dissolution of the Sb$_2$Se$_3$ layer at the Sb$_2$Se$_3$-CdS interface in the CdS-CSS device, resulting in the formation of large voids ($\approx$300 nm thick) across almost the entire interface region. Smaller voids were seen in the CdS-TE device, and none were observed

in the TiO_2 films.

EDX analysis showed significant diffusion of Sb and Se into the emitter layer of the CdS-CSS device. Se diffusion resulted in the formation of a Cd(S,Se) layer, which would have contributed to parasitic absorption and acted as a barrier to charge carrier transport, reducing cell efficiency. The interdiffusion was significantly suppressed in the TE cell, due to the lower deposition temperature. No diffusion was observed in the TiO_2 devices, despite the higher CSS growth temperature.

In all 4 samples, the mean orientation of the nanoribbons was found to be within a standard deviation of one another and around 30-50°. For samples A, C, D (i.e. CdS-CSS, and both TiO_2 devices) this was in good agreement with XRD data. However, for sample B (CdS-TE) XRD data predicts a large number of grains oriented such that the nanoribbons lie parallel to the substrate. This was not observed, perhaps because of the small sample size in electron diffraction. For the two CSS devices, the relationship between grain orientation and size was investigated. For the TiO_2 CSS device, it was found that the larger grains were better oriented, perhaps because of the effect of the seed layer on growth and restructuring. The fact that the ribbons are tilted relative to the substrate means that rather than there being Van der Waals gaps at grain boundaries the ribbons terminate there, potentially resulting in dangling covalent bonds that act as recombination centres.

5.2   Further Work

There are a number of avenues which could be explored with regards to further work. Thorough electron microscopy analysis of a TiO_2 sample grown via a single stage CSS process would be beneficial for better understanding the effect of the seed layer upon grain orientation and morphology, as would analysis of a device grown on CdS from a seed layer. This would also provide information on how the seed layer affects interdiffusion, and help better understanding of the diffusion process.

Additional further work could be done in HREM and HAADF imaging. Imaging of the Sb_2Se_3-CdS interface would allow measurement of lattice mismatch and strain, which can be related to the energy of the interface for different orientations. This may provide information on why Sb_2Se_3 appears to favour an orientation of 30-40° relative to the surface normal. HAADF imaging could also be applied to the grain boundaries to understand the defects arising where the ribbons terminate. DFT (density functional theory) work could

then be carried out to understand the effect that these defects have on band gap states and consequently recombination losses in the device.

References

[1] IPCC, 'Climate Change 2013: The Physical Science Basis. Contribution of Working Group I to the Fifth Assessment Report of the Intergovernmental Panel on Climate Change' [T.F. Stocker, D. Qin, G.-K. Plattner, M. M. B. Tignor, S. K. Allen, J. Boschung, A. Nauels, Y. Xia, V. Bex, P. M. Midgley (eds.)], (Cambridge University Press, 2013).

[2] European Environment Agency, Sectoral greenhouse gas emissions by IPCC sector, https://www.eea.europa.eu/data-and-maps/daviz/change-of-co2-eq-emissions-2#tab -dashboard-01 (accessed 25/04/19).

[3] M. Z. Jacobson, M. A. Delucchi, Energy Policy, 39, 1154-1169, (2011).

[4] IEA, Statistics, World electricity and heat for 2016, https://www.iea.org/statistics/?country=WORLD&year=2016&category=Electricity &indicator=ElecGenByFuel&mode=table&dataTable=ELECTRICITYANDHEAT (accessed 25/04/19).

[5] Fraunhofer ISE and PSE GmbH, Photovoltaics Report, https://www.ise.fraunhofer.de/content/dam/ise/de/documents/publications/studies/ Photovoltaics-Report.pdf (accessed 07/01/19)

[6] J. Nelson, 'The Physics of Solar Cells', Chapters 1, 8, and 10, (Imperial College Press, 2004).

[7] D. Neamen, 'An Introduction to Semiconductor Devices', Chapter 5, (McGraw-Hill, 2006).

[8] A. Shah, P. Torres, R. Tscharner, N. Wyrsch, H. Keppner, Science, **285**(5428), 692-698, (1999).

[9] W. Shockley, H.J. Queisser, J. Appl. Phys. **32**:3, 510-519, (1961).

[10] S. Rühle, Solar Energy, **130**, 139-147, (2016).

[11] T. Zdanowicz, T. Rodziewicz, M. Zabkowska-Waclawek, Solar Energy Materials & Solar Cells, **87**, 757-769, (2005).

[12] J. Wysocki, P. Rappaport, J. Appl. Phys. **31**:3, 571-578, (1960).

[13] G. P. Smestad, 'Optoelectronics of Solar Cells', Chapter 3, (Bellingham, 2002).

[14] C.H. Henry, J. Appl. Phys. **51**:8, 4494-4500, (1980).

[15] L. Yu, A. Zunger, Phys. Rev. Lett., **108**, 068701, (2012).

[16] G.L. Araújo, A. Marti, Sol. Energy Mater. Solar Cells, **33**, 213-240, (1994).

[17] National Renewable Energy Laboratory (NREL), Best Research-Cell Efficiencies, https://www.nrel.gov/pv/assets/pdfs/pv-efficiency-chart.20190103.pdf, (accessed 07/01/2019).

[18] M. Cardona, F. H. Pollak, Phys. Rev., **142**:2, 530-543, (1966).

[19] D.A. Cusano, Solid-State Electronics, **6**, 217-232, (1963).

[20] V. L. Deringer, R. P. Stoffel, M. Wuttig, R. Dronkowski, Chem Sci, **6**, 5255-5262, (2016).

[21] M. S. Leite, M. Abashin, H. J. Lezec, A. Gianfrancesco,. A. A. Talin, N. B. Zhitenev, ACS Nano, **8**:11, 11883-11890, (2014).

[22] M. Gloeckler, J.R. Sites, Journal of Physics and Chemistry of Solids, **66**, 1891-1894, (2005).

[23] S. B. Zhang, S.-H. Wei, A. Zunger, H. Katayama-Yoshida, Phys. Rev. B, **57**:16, 9642-9656, (1998).

[24] R. Baier, C. Leendertz, D. Abou-Ras, M. Ch. Luz-Steiner, S. Sadewasser, Sol. Energy. Mater. Sol. Cells, **130**, 124-131, (2014).

[25] Z. Chen, F. Chen, and N. Tan, J. Mater. Sci.: Mater. Electron. **26**:2, 970977, (2015).

[26] Y. Zhou, M. Leng, Z. Xia, J. Zhong, H. Song, X. Liu, B. Yang, J. Zhang, J. Chen, and K. Zhou, Adv. Energy Mater. **4**:8, 1301846, (2014).

[27] Y. Zhou, L. Wang, S. Chen, S. Qin, X. Liu, J. Chen, D.-J. Xue, M. Luo, Y. Cao, Y. Cheng, E. H. Sargent, J. Tang, Nature Photonics, **9**, 409-415, (2015).

[28] Y. Zhou, Y. Li, J. Luo, D. Li, X. Liu, C. Chen, H. Song, J. Ma, D.-J. Xue, B. Yang, J. Tang, Appl. Phys. Lett.**111**, 13901, (2017).

[29] D.-B. Li, X. Yin, C. R. Grice, L. Guan,Z. Song,C. Wang, C. Chen, K. Li, A. J. C, R. A. Awni, D. Zhao, H. Song, W. Tang, Y. Yan, J. Tang, Nano Energy **49**, 346-353, (2018).

[30] F. Kosek, J. Tulka, and L. Toura, Czech. J. Phys. **28**:3, 325-330, (1978).

[31] C. Chen, W. Li, Y. Zhou, C. Chen, M. Luo, X. Liu, K. Zeng, B. Yang, C. Zhang, J. Han, J. Tang, Appl. Phys. Lett. **107**, 043805, (2015).

[32] G. Ghosh, J. Phase Equilib. **14**:6, 753-763, (1993).

[33] S. Messina, M. T. S. Nair, and P. K. Nair, J. Electrochem. Soc., **156**:5, H327-H332, (2009).

[34] M. Calixto-Rodriguez, H. M. Garcia, M. T. S. Nair, and P. K. Nair, ECS J. Solid State Sci. Technol., **2**:4, Q69-Q73, (2013)

[35] Y. Rodríguez-Lazcano, Y. Peña, M. T. S. Nair, and P. K. Nair, Thin Solid Films, **493**:1-2, 77-82, (2005).

[36] A. Polman, M. Knight, E. C. Garnett, B. Ehrler, W. C. Sinke, Photovoltaic Materials: Present Efficiencies and Future Challenges, Science **352**:6283, aad4424-1, (2016).

[37] C. Chen, L. Wang, L. Gao, D. Nam, D. Li, K. Li, Y. Zhao, C. Ge, H. Cheong, H. Liu, H. Song, J. Tang, ACS Energy Lett. **2**, 2125-2132, (2017).

[38] L. J. Phillips, C. N. Savory, O. S. Hutter, P. J. Yates, H. Shiel, S. Mariotti, L. Bowen, M. Birkett, K. Durose, D. O. Scanlon, J. D. Major, IEEE J. Photovolt. **9**:2, 544-551, (2019).

[39] M. Luo, M . Leng, X. Liu, J. Chen, C. Chen, S. Qin, J. Tang, Appl. Phys. Lett. **104**, 173904, (2014).

[40] X. Wen, C. Chen, S. Lu, K. Li, R. Kondrotas, Y. Zhao, W. Chen, L. Gao, C. Wang, J. Zhang, G. Niu, J. Tang, Nat. Commun., **9**:2179, (2018).

[41] Z. Li, X. Liang, G. Li, H. Liu, H. Zhang, J. Guo, J. Chen, K. Shen, X. San, W. Yu, R. E. I. Schropp, Y. Mai, Nat. Commun., **10**:125, (2019).

[42] L. Wang, D.-B. Li, K. Li, C. Chen, H.-X. Deng, L. Gao, Y. Zhao, F. Jiang, L. Li, F. Huang, Y. He, H. Song, G. Niu, J. Tang, Nat. Energy **2**, 17046, (2017).

[43] S. G. Kumar, K. K. Rao, Energy Environ. Sci., **7**:1, 45102, (2014).

[44] X. Liu, J. Chen, M. Luo, M. Leng, Z. Xia, Y. Zhou, S. Qin, D.-J. Xue, L. Lv, H. Huang, D. Niu, J. Tang, Appl. Mater. Interfaces, **6**, 10687-10685, (2014).

[45] O. S. Hutter, L. J. Phillips, K. Durose, J. D. Major, Sol. Energy Mater. Sol. Cells, **188**, 177-181, (2018).

[46] R. J. Martin Palma, 'Nanotechnology: A Crash Course', Chapter 4, (SPIE, 2010).

[47] R. C. Jaeger, 'Introduction to microelectronic fabrication', Chapter 6, (Addison-Wesley, 1988).

[48] B. R. Wakeling, 'Close space sublimation of CdTe for solar cells and the effect of underlying layers', (PhD Thesis, Cranfield University, Cranfield, United Kingdom, 2010).

[49] P. B. Barna, M. Adamik, Thin Solid Films, **317**, 27-33, (1998).

[50] C. Potamialis et al, 2016. Fabrication of CdTe thin films by close space sublimation. IN: M. Hutchins, R. Treharne, and A. Cole (eds.) 12th Photovoltaic Science, Application and Technology Conference C98 (PVSAT-12), University of Liverpool, 6-8th April, pp. 199-202.

[51] H. Nagayoshi and K. Suzuki, in IEEE Nuclear Science Symposium Conference Record (2004), vol. 1-7, p. 4411.

[52] T. Okamoto, Y. Harada, A. Yamada, and M. Konagai, Solar Energy Materials and Solar Cells, **67**, 187-194 (2001).

[53] T. C. Anthony, A. L. Fahrenbruch, and R. H. Bube, Journal of Vacuum Science & Technology A-Vacuum Surfaces And Films, **2**, 1296-1302 (1984).

[54] J. D. Major, Y. Y. Proskuryakov, K. Durose, G. Zoppi, I. Forbes, Sol. Energy Mater Sol. Cells **94**, 1107-1112, (2010).

[55] P. J. Yates, 'Emerging Absorber Materials for Sustainable Photovoltaics', (PhD Thesis, University of Liverpool, Liverpool, 2018).

[56] W. Zhou, R. Apkarian, Z. L. Wang, D. Joy, 'Fundamentals of Scanning Electron Microscopy (SEM)', *Scanning Microscopy for Nanotechnology: Techniques and Applications*, W. Zhou, Z. L. Wang, (Springer, 2010).

[57] D. B. Williams, C. B. Carter, 'Transmission Electron Microscopy: A Textbook for Materials Science', Vol. I-III, (Plenum Press, 1996).

[58] P. J. Goodhew, F. J. Humphreys, R. Beanland, 'Electron Microscopy and Analysis', (CRC Press, 2014).

[59] M. H. Loretto, 'Electron Beam Analysis of Materials', (Chapman & Hall, 1994).

[60] C. A. Volkert, A. M. Minor, MRS Bulletin, **32**:5, 389-399, (2007).

[61] N. Yao, 'Introduction to the focused ion beam system', *Focused Ion Beam Systems: Basics and Applications*, N. Yao, (Cambridge University Press, 2010).

[62] R. J. D. Tilley, 'Crystals and Crystal Structures', Chapter 2, (Wiley, 2006).

[63] S. Horiuchi, 'Fundamentals of High Resolution Transmission Electron Microscopy', Chapter 6, (North-Holland, 1994).

[64] R. J. Keyse, A. J. Garratt-Reed, P. J. Goodhew, G. W. Lorimer, 'Introduction to Scanning Transmission Electron Microscopy', Chapters 1 and 4, (BIOS Scientific, 1998).

[65] I. P. Jones, 'Chemical Microanalysis Using Electron Beams', Chapters 1-4 and Appendix A, (The Institute of Materials, 1992).

[66] M. Schaffer, B. Schaffer, Q. Ramasse, Ultramicroscopy, **114**, 62-71, (2012).

[67] D. A. Porter, K. E. Easterling, M. Y. Sherif, 'Phase Transformations in Metals and Alloys', Chapter 2, (CRC Press, 2009).

[68] H. Sowa, Solid State Sciences, **7**, 1384-1389, (2005).

[69] H. Sowa, Solid State Sciences, **7**, 73-78, (2005).

[70] Q. Dai, Y. Song, D. Li, H. Chen, S. Kan, B. Zhou, Y. Wang, Y. Deng, Y. Hou, S. Yu, L. Chen, B. Liu, G. Zou, Chem. Phys. Lett., **439**:1-3, 65-68, (2007).

[71] C. Chen, D. Bobela, Y. Yang, S. Lu, K. Zeng, C. Ge, B. Yang, L. Gao, Y. Zhao, M. Beard, J. Tang, Front. Optoelectron., **10**:1, 18-30, (2017).